Seismic stability of a circular tunnel in cohesive-frictional soils using a stable node-based smoothed finite element method

1 author:

Hoang Nguyen
Imperial College London

Vol. 128, October 2022

ISSN 0886-7798

Original research, innovations and case studies in the development of tunnelling, trenchless technology and underground space

Tunnelling and Underground Space Technology

incorporating **Trenchless Technology Research**

- geo-investigation
- underground mapping
- planning
- regulation
- design
- construction
- operation
- maintenance

www.elsevier.com

Available online at www.sciencedirect.com

ScienceDirect

Seismic stability of a circular tunnel in cohesive-frictional soils using a stable node-based smoothed finite element method

T. Vo-Minh[a*], **H. C. Nguyen**[b]
[a*]Faculty of Civil Engineering, Hutech University, Ho Chi Minh City, Vietnam.
[b]Department of Civil and Industrial Design, University of Liverpool, Liverpool, UK.

E-mail: [a*]*vm.thien@hutech.edu.vn*, [b]*H.C.Nguyen@liverpool.ac.uk*.

Abstract. This paper presents the effect of horizontal and vertical earthquake force on the stability of a single circular tunnel in cohesive-frictional soils using a stable node-based smoothed finite element method (SNS-FEM). In this study, seismic forces are computed as horizontal and vertical pseudo-static body forces arising on the soil and additional inertial forces associated with the uniform surcharge applied to the ground surface. In the upper bound limit analysis based on SNS-FEM, the soil behaviour is described as rigid-perfectly plastic materials, and plasticity deformation obeys the associated flow rule following the Mohr-Coulomb failure criterion. Firstly, the numerical results were checked against other numerical solutions in the literature. The present results agree with prior contributions, proving that the proposed approach can give efficient and reliable solutions to the stability number. Secondly, the variations of the seismic stability number with changes in the horizontal earthquake acceleration coefficient were intensively investigated for different values of soil properties, internal friction angle and the depth-to-diameter ratio of the tunnel. It is shown that the seismic stability numbers of circular tunnels reduce remarkably with the increase of horizontal seismic coefficient and the soil weight. Thirdly, the seismic stability numbers were summarised in design charts for practical use in geotechnical engineering.

Keywords: Circular tunnel, Limit analysis, SNS-FEM, SOCP, Seismic stability, Seismic force.

1. Introduction

Due to rapid urbanization and society's need, there has been an increase in the demand for constructing more underground circular tunnels for highways, railways, water supply, and metro projects. In addition, tunnels are now being built in high seismic zones with soft ground conditions, mainly in cohesive-frictional soils. Calculating the tunnel's seismic stability is vital for practising engineers. Therefore, it is desirable to perform more research to understand further the behaviour of tunnels subjected to seismic loading.

Extensive studies on the stability of circular tunnels were performed at Cambridge during the 1970s using theoretical and empirical techniques. Notably, Atkinson and Pott (1977) conducted centrifuge tests for a circular tunnel in cohesionless soils supported by compressed air. Seneviratne (1979) and Mair (1979) then performed centrifuge model tests of shallow tunnels in soft clay to determine the internal pressure required to maintain circular tunnels' stability. In addition, Wu and Lee (2003) performed centrifuge model tests in clay soils to estimate the ground movement and the failure mechanism of single and two parallel circular tunnels. Recently, Kirsch (2010) and Gregor et al. (2011) carried out small-scale model tests by the 1g shake table test (where g is the acceleration due to gravity) to determine the face stability of a circular tunnel in sandy soil.

Drucker et al. (1952) first proposed the limit analysis based on the plastic bound theorems, and Chen (1975) applied this approach to evaluate the stability of geotechnical problems. Then, by employing the upper bound limit analysis using the rigid-block failure mechanism and lower bound theorem, Davis et al. (1980), Mühlhaus (1985), and Leca and Dormieux (1990) investigated the collapse load and the failure of a circular tunnel in cohesive-frictional soils.

A combination of limit analysis and finite element method has offered powerful tools to compute the stability of geotechnical problems with complicated geometry and boundary conditions. Sloan and Assadi (1991) first examined the undrained stability of a square tunnel in soil, considering variations in cohesion with depth using classical upper and lower bound limit analysis. Lyamin and Sloan (2000) and Lyamin et al. (2001) investigated the stability of circular and square tunnels in cohesive-frictional soils based on nonlinear analysis and finite element limit analysis (FELA). Yang and Yang (2010) calculated the support pressure for a shallow rectangular tunnel in cohesive-frictional soil using the rigid-block failure mechanisms and finite upper bound solutions. Wilson et al. (2011) considered a circular tunnel's undrained stability in clay with the variation in cohesion with depth. Using finite element upper bound and lower bound limit analysis, Yamamoto et al. (2011a, 2011b) investigated circular and square tunnels' stability in cohesive-frictional soils subjected to surcharge loading. Khezri et al. (2015) used the upper bound limit analysis incorporating the linear variation of the soil cohesion with depth to calculate the tunnel face's pressure to maintain a circular tunnel's stability. Using the kinematic theorem, T. Vo-Minh et al. (2017a, 2017b, 2018) used the node-based smoothed finite element method (NS-FEM) and second-order cone programming (SOCP) to investigate the stability of two circular and dual square tunnels in cohesive-frictional soils. More recently, Nguyen (2021a, 2021b) adopted the smoothed finite element limit analysis (ES-FEM, CS-FEM and NS-FEM) to assess the seismic effects on the stability of tunnels, producing very satisfactory results of the stability number when compared with the use of classical finite element limit analysis.

In recent decades, a few researchers investigated circular tunnels' stability in cohesive-frictional soils subjected to the influence of seismic forces. Cilingir and Madabhushi (2011) conducted the centrifuge test and finite element analysis to consider depth effects on the seismic response of circular tunnels subjected to transverse shear waves in soft ground. Tsinidis et al. (2013) described the numerical simulation of the round-robin numerical test on tunnels and compared those with the experimental data, soil surface settlements, soil shear strains, and dynamics of internal forces of the tunnel lining. Wang et al. (2013) calculated the seismic response of the soil-structure interaction between underground structure and nearby pile-supported structure on viscous-elastic soil layer. Recently, Abate et al. (2019a, 2019b) investigated the role of shear wave velocity, damping ratio and non-linearity of soil in the seismic response of a coupled tunnel-soil-above ground building system. By employing the upper and lower bound finite element limit analysis, Sahoo and Kumar (2012) and Chakraborty and Kumar (2013) investigated the maximum unit weight of soil mass that the tunnel can stabilise under the presence of horizontal pseudo-static earthquake body forces without the need to internal support. Sahoo and Kumar (2014) computed the support pressure required to maintain circular tunnels' stability with seismic body forces' inclusion using upper bound finite element limit analysis combined with a linear optimization technique. Banerjee and Chakraborty (2016) used the lower bound finite element limit analysis to calculate a circular tunnel's stability subjected to seismic body forces underneath a sloping ground surface. Zi-hong et al. (2019) recently presented an analytical method to evaluate tunnel collapse mechanisms during earthquakes based on the horizontal slice and variational principles. According to this paper, the tunnel radius and the surrounding soil cohesion are the two most important factors influencing tunnel stability.

In recent years, the finite element method (FEM) has been a practical approach for solving the limit analysis of geotechnical problems. However, the drawback of the traditional FEM is a volumetric locking problem for a purely cohesive material. Liu et al. (2009) first proposed the node-based smoothed finite element method (NS-FEM) for upper-bound solutions to solid mechanics problems to overcome this phenomenon. A group of node-based smoothed finite element methods (NS-FEM) using the node-based strain smoothing technique have been developed for 3D heat transfer analysis (Wu et al., 2009), fracture problems (Liu et al., 2010), upper bound analysis of visco-elastoplastic of solid problems (Nguyen-Thoi et al., 2010), adaptive analysis (Nguyen-Thoi et al., 2011; Tang et al., 2011), computational of limit load and shakedown of solid problems (Nguyen-Xuan et al., 2012). Mohapatra and Kumar (2019) recently employed different smoothed finite element methods (S-FEM) for the kinematic limit analysis to solve plane strain and plane stress stability problems using the Mohr-Coulomb yield criterion.

It is worth mentioning that the original NS-FEM still has temporal instability for dynamic problems, transient analysis and acoustic problems. Therefore, a stable node-based smoothed finite element method (SNS-FEM) was developed for the analysis of acoustic problems (Wang et al., 2015), static and dynamic analysis of solid mechanics (Feng et al., 2016), metal forming problems (Yang et al., 2019). Using SNS-FEM, the problem domain is discretized by three-node triangular elements. The smoothed Galerkin weak form is then used to establish the discretized system equation, and the node-based smoothing technique is employed to perform the smoothing operation. Based on the original NS-FEM, the smoothing domain's shape function was first carried out within each smoothing domain as in NS-FEM. Then, the smoothed shape function gradient was expanded using the Taylor equation's first order in an approximation integral domain. Four additional integration points (for 2D space) or six additional integration points (for 3D space) were proposed to modify the smoothed strain.

It is widely accepted that SNS-FEM has been successfully applied to several fields, including structural mechanics, solid mechanics, acoustic analysis, and electromagnetic problems, in recent years. However, few researchers applied this numerical method for upper bound limit analysis in geomechanical problems. Vo-Minh and Nguyen-Son (2021) recently applied SNS-FEM to investigate two circular tunnels' stability at different depths in cohesive-frictional soils based on the upper bound limit analysis. This study adopted a stable node-based smoothed finite element method for calculating the seismic stability of circular tunnels in cohesive-frictional soils subjected to surcharge loadings (Nguyen and Nguyen-Son, 2022; Nguyen and Vo-Minh, 2022a, 2022b). In general, the reduction of the stability numbers of circular tunnels is attributed to the following factors:

1. the degradation of the shear strength due to earthquakes,
2. the rising inertia forces in the soil mass, and
3. inertia forces associated with the surcharge.

We investigates changes in a circular tunnel's seismic stability numbers with lateral and vertical seismic accelerations. In addition, the corrective factors are computed to quantify the reduction in a circular tunnel's stability results due to the soil inertia and the inertial forces associated with the surcharges. Several numerical examples are compared with reference solutions to verify the accuracy and reliability of the proposed method.

This paper is arranged as follows: Section 2 describes the problem definition. Section 3 summarizes a stable node-based smoothed finite element for the upper bound limit analysis problem. In section 4, some numerical examples are performed and discussed to demonstrate the presented method's effectiveness. Finally, some concluding remarks are made in section 5.

2. Problem definition

Fig.1 shows the problem definition and the boundary of a plane strain circular tunnel in cohesive-frictional soils. The circular tunnel has a diameter of D and is located at a depth of H from the horizontal ground surface. The rectangular domain is chosen sufficiently far from the tunnel periphery, with the width $2L$ and the height $B = H + D + d$, shown in Fig. 1. In this study, the values of L from $3D$ to $10D$, H varied in the range of H= D – $5D$, d varied between D and $2D$ are considered to ensure that the failure mechanism is inside the domain, eliminating the effect of boundary on the numerical results. The circular tunnel's soil is cohesive-frictional materials, obeying the associated flow rule and Mohr-Coulomb yield criterion with cohesion c, friction angle ϕ and unit weight γ.

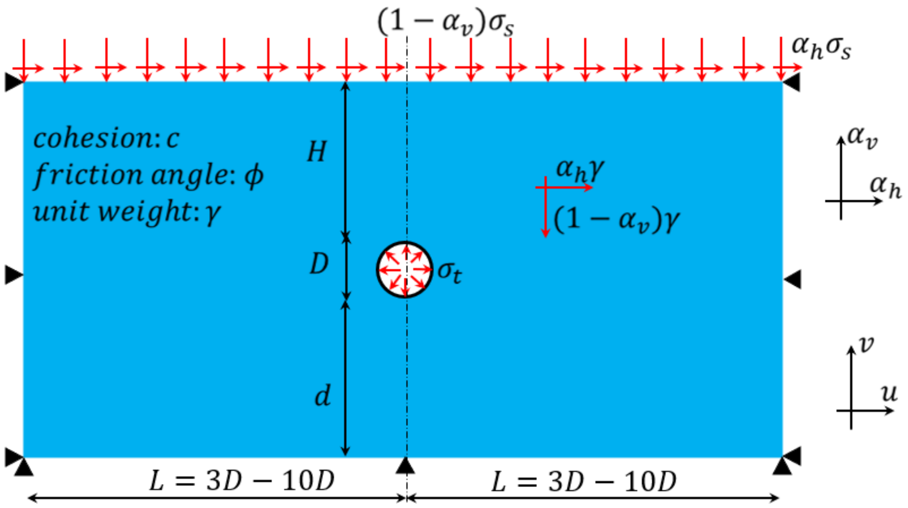

Fig. 1 The geometry and boundary conditions of a circular tunnel subjected to the surcharge and seismic forces

A circular tunnel is subjected to the vertical surcharge loading $(1-\alpha_v)\sigma_s$ and the horizontal surcharge $\alpha_h\sigma_s$ on the ground surface, as illustrated in Fig. 1. In the pseudo-static analysis, the dynamic loading induced by the earthquake is considered time-independent, which ultimately assumes that the horizontal and the vertical earthquake acceleration coefficients α_h, α_v are uniform throughout the soil layer. In this paper, a dimensionless stability number σ_s/c is defined by using a functional relationship of ϕ, $\gamma D/c$, H/D, α_h and α_v such that

$$\frac{\sigma_s}{c} = f\left(\frac{H}{D}, \alpha_h, \alpha_v, \frac{\gamma D}{c}, \phi\right) \tag{1}$$

In this study, the tunnel diameter ratio to its depth H/D = 1, 3, 5, and the horizontal earthquake acceleration coefficient α_h varies from 0 to 0.5 is considered. In addition, the soil properties $\gamma D/c$ range from 0 to 2, and the value of friction angle ϕ varies from 0° to 35°. To consider the effect of both horizontal and vertical components of the seismic acceleration on stability number σ_s/c, the values of the ratio α_v/α_h from -1 to 1 are used in the analyses. In the upper bound limit analysis using SNS-FEM, the horizontal displacements between the ground surface and the surcharge loading are free ($u \neq 0$) to describe a smooth interface condition.

3. A stable node-based smoothed finite element method (SNS-FEM) for upper bound limit analysis

3.1. A short introduction to a stable node-based smoothed finite element method (SNS-FEM)

Unlike the traditional finite element method (FEM), the numerical integration domains of the node-based smoothing method (NS-FEM) are based on polygonal cells related to the nodes rather than the elements. The problem domain Ω is divided into N_s smoothing cells formulated as $\Omega = \sum_{k=1}^{N_s} \Omega_k^s$ and $\Omega_i^s \cap \Omega_j^s = \varnothing$, $i \neq j$ and N_s is the total number of field nodes in the entire problem domain. The polygonal cells, Ω_k^s, called a nodal smoothing domain associated with the node k, are constructed by connecting the mid-edge points sequentially to the centroid of surrounding triangular elements, as shown in Fig. 2. The smoothing domain boundary Ω_k^s is labelled as Γ_k, and the union of all Ω_k^s forms precisely the whole problem **Ω**.

The smoothed strain on the cell Ω_k^s associated with node k using NS-FEM can be calculated by

$$\tilde{\boldsymbol{\varepsilon}}_k = \sum_{k \in N^{(s)}} \tilde{\mathbf{B}}_k(\mathbf{x}_s)\mathbf{d}_k \tag{2}$$

where $N^{(s)}$ is the set containing nodes directly connected to node k, $\mathbf{d}_k$ is the nodal displacement vector and the smoothed strain gradient matrix $\tilde{\mathbf{B}}_k(\mathbf{x}_s)$ on the domain Ω_k^s can be determined from

$$\tilde{\mathbf{B}}_k(\mathbf{x}_s) = \begin{bmatrix} \tilde{b}_{kx}(x_s) & 0 \\ 0 & \tilde{b}_{ky}(x_s) \\ \tilde{b}_{ky}(x_s) & \tilde{b}_{kx}(x_s) \end{bmatrix} \tag{3}$$

where

$$\tilde{b}_{kh}(x_s) = \frac{1}{A_k^{(s)}} \int_{\Gamma_k} \mathbf{n}_h^{(s)}(\mathbf{x}) N_k(\mathbf{x}) \mathrm{d}\Gamma \tag{4}$$

where $A_k^{(s)} = \int_{\Omega_k^s} d\Omega$ is the area of the cell Ω_k^s, $N_k(\mathbf{x})$ is the FEM shape function for node k, and $\mathbf{n}^{(s)}(\mathbf{x})$ is the normal outward vector on the boundary $\Gamma_k^{(s)}$. The number of Gauss points for line integration (4) depends on the degree of N_k. If N_k are linear shape functions, one Gauss point is sufficient for line integration along each segment of a boundary of $\Gamma_k^{(s)}$ of Ω_k^s, Eq. (4) can be transformed to its algebraic form

$$\tilde{b}_{kh}(x_s) = \frac{1}{A_k^{(s)}} \sum_{k=1}^{M} \mathbf{N}_k(\mathbf{x}_k^{GP}) n_{kh}^{(s)} l_k^{(s)}, (h = x, y) \tag{5}$$

where M is the total of the boundary segment of $\Gamma_k^{(s)}$, $\mathbf{x}_i^{GP}$ is the Gauss point of the boundary segment of $\Gamma_k^{(s)}$, which has length $l_k^{(s)}$ and outward unit normal $n_{kh}^{(s)}$

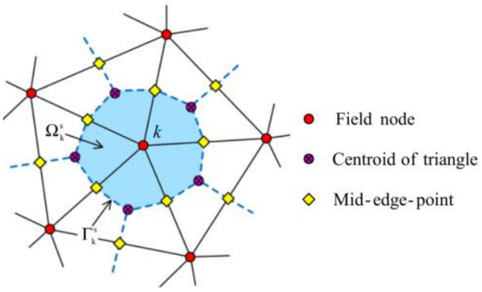

Fig. 2. The smoothing cells associated with the nodes in the NS-FEM

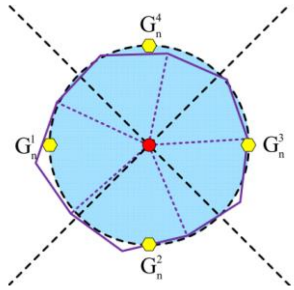

Fig. 3. The approximate integration domain and integration points for SNS-FEM

Although NS-FEM is applied well in many fields, NS-FEM has some drawbacks to ensure stability and accuracy in large deformation and time-dependent problems. The temporal instability caused by its non-zero energy model has been investigated by researchers (Wang et al., 2015; Feng et al., 2016; Yang et al., 2019). To overcome the disadvantage of NS-FEM, a stable item is introduced by considering the smoothed strain field's variance to ensure the accuracy and stability of results. Fig. 3 shows the approximate integration domain and integration points for SNS-FEM for a 2D problem. The node integral smooth domain $\Omega_k{}^s$, which is an integral region formed by all the element domains of node *k* is approximated to a circle with the same area, and a stable node smooth domain $\Omega_k{}^{sc}$ is obtained. Then $\Omega_k{}^s$ is divided into four subdomains to obtain four integral points. The four integration points $G_n{}^i$ (i = 1, 2, 3, 4) are the intersections of the coordinate axis of the local coordinate system and the boundary of the stable node integral smooth domain $\Omega_k{}^{sc}$, as shown in Fig. 3. The radius of the equivalent circle is defined by

$$r_c = \sqrt{\frac{A_k^s}{\pi}} \tag{6}$$

where $A_k^{(s)}$ is the area of the cell $\Omega_k{}^s$

Assuming smoothing strain in $\Omega_k{}^{sc}$ is continuous and derivable at the first order, its Taylor expansion can be expressed as

$$\tilde{\boldsymbol{\varepsilon}} = \tilde{\boldsymbol{\varepsilon}}_k + \frac{\partial \tilde{\boldsymbol{\varepsilon}}}{\partial x}(x - x_k) + \frac{\partial \tilde{\boldsymbol{\varepsilon}}}{\partial y}(y - y_k) \tag{7}$$

Therefore, the smoothed strains of the four-domains $\tilde{\boldsymbol{\varepsilon}}_1^{sc}, \tilde{\boldsymbol{\varepsilon}}_2^{sc}, \tilde{\boldsymbol{\varepsilon}}_3^{sc}, \tilde{\boldsymbol{\varepsilon}}_4^{sc}$ are

$$\tilde{\boldsymbol{\varepsilon}}_1{}^{sc} = \tilde{\boldsymbol{\varepsilon}}_k - \frac{\partial \tilde{\boldsymbol{\varepsilon}}}{\partial x} r_c\,;\ \tilde{\boldsymbol{\varepsilon}}_2{}^{sc} = \tilde{\boldsymbol{\varepsilon}}_k - \frac{\partial \tilde{\boldsymbol{\varepsilon}}}{\partial y} r_c\,;\ \tilde{\boldsymbol{\varepsilon}}_3{}^{sc} = \tilde{\boldsymbol{\varepsilon}}_k + \frac{\partial \tilde{\boldsymbol{\varepsilon}}}{\partial x} r_c\,;\ \tilde{\boldsymbol{\varepsilon}}_4{}^{sc} = \tilde{\boldsymbol{\varepsilon}}_k + \frac{\partial \tilde{\boldsymbol{\varepsilon}}}{\partial y} r_c \tag{8}$$

The modified smoothing strain around node *k* can be calculated following Eq. (7) for 2D solid mechanics problems

$$\hat{\boldsymbol{\varepsilon}}_k = \tilde{\boldsymbol{\varepsilon}}_k + (\tilde{\boldsymbol{\varepsilon}}_k{}^{sc})_x^{\mathrm{T}} (\tilde{\boldsymbol{\varepsilon}}_k{}^{sc})_x \cdot \frac{A_k^s}{2} + (\tilde{\boldsymbol{\varepsilon}}_k{}^{sc})_y^{\mathrm{T}} (\tilde{\boldsymbol{\varepsilon}}_k{}^{sc})_y \cdot \frac{A_k^s}{2} \tag{9}$$

Note that the four integration points in the SNS-FEM are just temporary variables, which is accomplished equivalently by one point integration and the stabilization terms. Therefore, only a slight modification of the original NS-FEM code is revised.

3.2. An upper bound limit analysis for a plane strain with Mohr-Coulomb yield criterion using SNS-FEM

A two-dimensional problem domain Ω bounded by a continuous boundary $\Gamma_{\dot{\mathbf{u}}} \cup \Gamma_{\mathbf{t}} = \Gamma$, $\Gamma_{\dot{\mathbf{u}}} \cap \Gamma_{\mathbf{t}} = \varnothing$ is considered. The rigid-perfectly plastic body is subjected to external tractions $\mathbf{g}$ on $\Gamma_{\mathbf{t}}$ and body forces $\mathbf{f}$ on the boundary $\Gamma_{\dot{\mathbf{u}}}$ prescribed by the displacement velocity vector $\dot{\mathbf{u}}$. The strain rates can be expressed by equation

$$\dot{\boldsymbol{\varepsilon}} = \begin{bmatrix} \dot{\varepsilon}_{xx} & \dot{\varepsilon}_{yy} & \dot{\gamma}_{xy} \end{bmatrix}^T = \nabla \dot{\mathbf{u}} \tag{10}$$

In the upper bound theorem, a kinematically admissible displacement field $\dot{\mathbf{u}} \in U$, such that

$$W_{\mathrm{int}}(\boldsymbol{\sigma}, \dot{\mathbf{u}}) = \alpha^+ W_{\mathrm{ext}}(\dot{\mathbf{u}}) \tag{11}$$

where α^+ is the limit load multiplier of the external tractions load $\mathbf{g}$ and body forces $\mathbf{f}$

The external work can be determined

$$W_{ext}(\dot{\mathbf{u}}) = \int_{\Omega} \mathbf{f}.\dot{\mathbf{u}} d\Omega + \int_{\Gamma_t} \mathbf{g}.\dot{\mathbf{u}} d\Gamma \tag{12}$$

The internal plastic dissipation of the two-dimensional domain Ω can be written as

$$W_{\mathrm{int}}(\boldsymbol{\sigma}, \dot{\mathbf{u}}) = \int_{\Omega} D_p(\dot{\mathbf{u}}) d\Omega = \int_{\Omega} \boldsymbol{\sigma}.\dot{\boldsymbol{\varepsilon}}.d\Omega \tag{13}$$

in which a space of kinematically admissible velocity field is denoted by

$$U = \left\{ \dot{\mathbf{u}} \in (H^1(\Omega))^2, \dot{\mathbf{u}} = \bar{\dot{\mathbf{u}}} \text{ on } \Gamma_{\dot{\mathbf{u}}} \right\} \tag{14}$$

Defining $C = \{\dot{\mathbf{u}} \in U \,|W_{ext}(\dot{\mathbf{u}}) = 1\}$, the limit analysis problem is based on the kinematical theorem to determine the collapse multiplier α^+ yielding the following optimization problem

$$\begin{aligned} &\alpha^+ = \max \left\{ \exists \boldsymbol{\sigma} \in \Sigma \middle| W_{\mathrm{int}}(\boldsymbol{\sigma}, \dot{\mathbf{u}}) = \alpha W_{ext}(\dot{\mathbf{u}}), \forall \dot{\mathbf{u}} \in U \right\} = \min_{\dot{\mathbf{u}} \in U} D_p(\dot{\mathbf{u}}) \\ &st \begin{cases} \dot{\mathbf{u}} = 0 & \text{on } \Gamma_u \\ W_{ext}(\dot{\mathbf{u}}) = 1 \end{cases} \end{aligned} \tag{15}$$

For plane strain in geotechnical problems, Makrodimopoulos and Martin (2006) proposed the internal plastic dissipation equation as follows

$$D_p(\dot{\mathbf{u}}) = c \cos\phi \int_{\Omega} \sqrt{\dot{\boldsymbol{\varepsilon}}^T \Theta \dot{\boldsymbol{\varepsilon}}} d\Omega \quad \text{with } \Theta = \begin{bmatrix} 1 & -1 & 0 \\ -1 & 1 & 0 \\ 0 & 0 & 1 \end{bmatrix} \tag{16}$$

where c, ϕ are the cohesion and friction angle of the soil, respectively.

For an associated flow rule, the plastic strain rates vector is given by

$$\dot{\boldsymbol{\varepsilon}} = \lambda \frac{\partial \psi(\boldsymbol{\sigma})}{\partial \boldsymbol{\sigma}} \tag{17}$$

where λ is a non-negative the plastic multiplier and the Mohr-Coulomb yield function $\psi(\boldsymbol{\sigma})$ can be expressed in the form of stress components as

$$\psi(\boldsymbol{\sigma}) = \sqrt{(\sigma_{xx} - \sigma_{yy})^2 + 4\tau_{xy}^2} + (\sigma_{xx} + \sigma_{yy}) \sin\phi - 2c \cos\phi \tag{18}$$

Using SNS-FEM, the domain is discretized by N_e triangular elements and the total number of nodes N_s. The stable smoothed strains rates $\hat{\boldsymbol{\varepsilon}}$ can be calculated from Eq. (9). The upper bound limit analysis for a plane strain in geomechanics problems using the Mohr-Coulomb failure criterion can be written

$$\alpha^{+} = \frac{\sigma_s}{c} = \min\left(\sum_{i=1}^{N_n} cA_i \cos\phi\sqrt{(\hat{\varepsilon}_{xx}^{i} - \hat{\varepsilon}_{yy}^{i})^2 + (\hat{\gamma}_{xy}^{i})^2}\right) = \min\left(\sum_{i=1}^{N_n} cA_i t_i \cos\phi\right)$$

$$st\begin{cases} \dot{\mathbf{u}} = 0 \quad \text{on } \Gamma_{\mathbf{u}} \\ W_{ext}(\dot{\mathbf{u}}) = 1 \\ \hat{\varepsilon}_{xx}^{i} + \hat{\varepsilon}_{yy} = t_i \sin\phi \\ t_i \ge \sqrt{(\hat{\varepsilon}_{xx}^{i} - \hat{\varepsilon}_{yy}^{i})^2 + (\hat{\gamma}_{xy}^{i})^2}, i = 1, 2, \ldots\ldots, N_n \end{cases} \tag{19}$$

where α^{+} is a stability number, A_i is the area of node i, N_n is the total number of nodes in the domain, c is the cohesion, ϕ is the internal friction angle of soil. The fourth constraint in Eq. (19) is the form of quadratic cones. As a result, the conic interior-point optimizer of the academic Mosek package (2009) is used for solving this problem. The computations were performed on a Dell Optiplex 990 (Intel Core^{TM} i5, 1.6GHz CPU, 8GB RAM) in a Windows XP environment. The SNS-FEM approach has been coded in the Matlab language.

4. Numerical examples and discussions

Fig. 4 shows the seismic stability problem of circular tunnel in cohesive-frictional soil in the case H/D = 1, $\gamma D/c$ = 1, $\phi = 10^{o}$ and α_h = 0.1, α_v = 0. The typical finite element meshes for a circular tunnel, deformed meshes and power dissipation are illustrated in Figs. 4a, 4b, 4c, respectively. This paper used GiD software to generate triangular elements with reduced element size close to the tunnel's periphery. The domain's size is assumed sufficiently large to eliminate the boundary effects and the plastic zones to be contained fully within the domain.

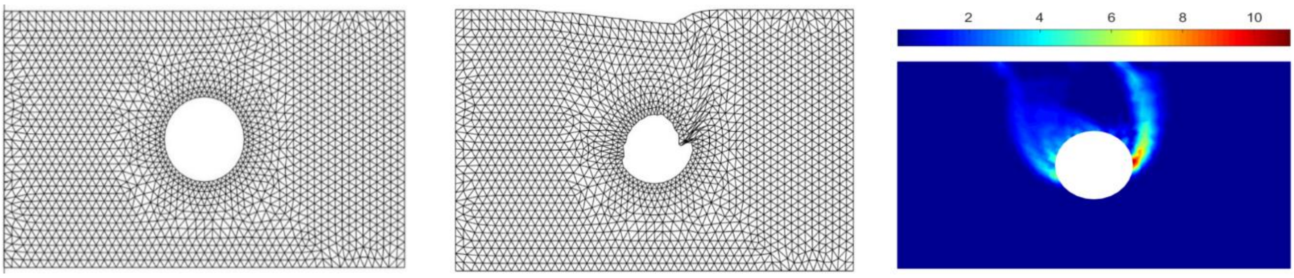

(a) Typical mesh (b) Deformed mesh (c) Power dissipation

Fig. 4. Seismic stability of circular tunnel for H/D = 1, $\gamma D/c$ = 1, $\phi = 10^{o}$, α_h = 0.1 and α_v = 0

4.1. Discussion of the failure mechanisms

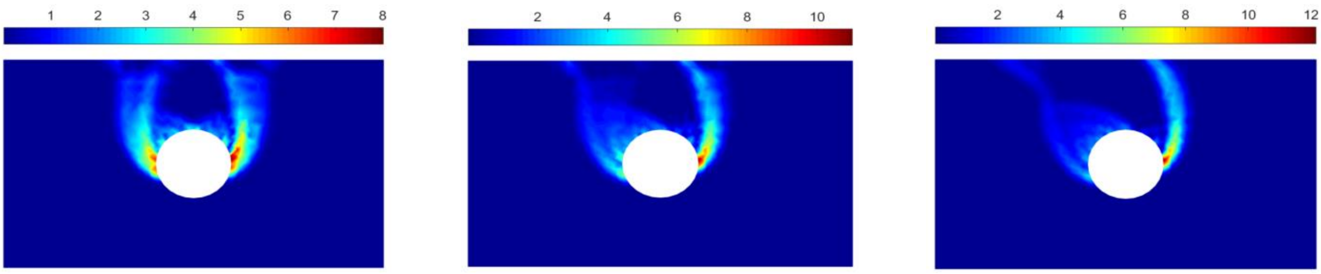

(a) α_h = 0 (b) α_h = 0.1 (c) α_h = 0.3

Fig. 5. Failure mechanism of circular tunnel for H/D = 1, $\gamma D/c$ = 1, α_v = 0, $\phi = 10^{o}$

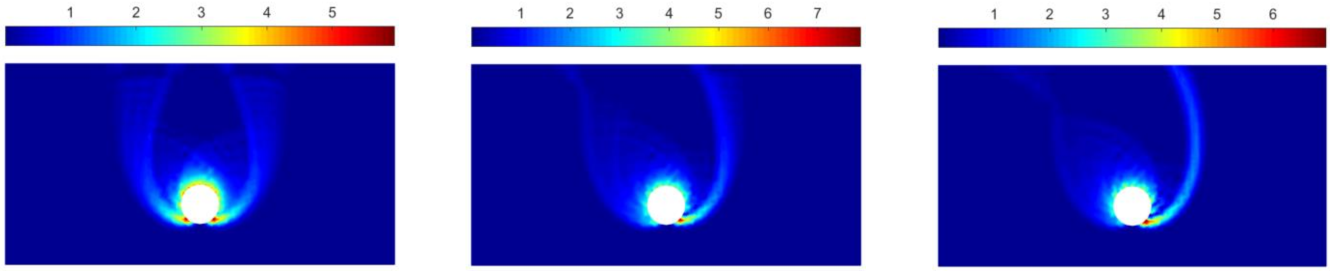

(a) $\alpha_h = 0$ (b) $\alpha_h = 0.1$ (c) $\alpha_h = 0.3$

Fig. 6. Failure mechanism of circular tunnel for $H/D = 3$, $\gamma D/c = 1$, $\alpha_v = 0$, $\phi = 10^o$

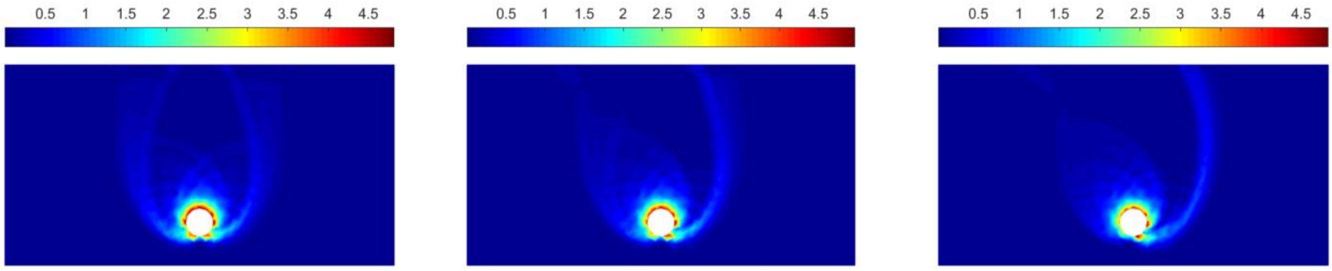

(a) $\alpha_h = 0$ (b) $\alpha_h = 0.1$ (c) $\alpha_h = 0.3$

Fig. 7. Failure mechanism of circular tunnel for $H/D = 5$, $\gamma D/c = 1$, $\alpha_v = 0$, $\phi = 10^o$

Figs. 5a, 6a, 7a show the power dissipation of a circular tunnel in the cases $H/D = 1, 3, 5$ and small friction angle $\phi = 10^o$ under static conditions ($\alpha_h = 0$, $\alpha_v = 0$). In Fig. 5a, the failure mechanism of a shallow circular tunnel is symmetrical about the vertical plane passing through the tunnel's centre. A slip surface originates from the middle part of the tunnel and extends up to the ground surface. In moderate tunnel $H/D = 3$ and deep tunnel $H/D = 5$, as shown in Figs. 6a and 7a, the failure mechanisms originate from the bottom of the tunnel and extend up to the ground surface.

Figs. 5b-5c, 6b-6c, 7b-7c illustrate the plastic dissipation distributions of a circular tunnel in the case $\gamma D/c = 1$, $\phi = 10^o$ for different combinations of $H/D = 1, 3, 5$ and α_h varies from 0.1 to 0.3. Under seismic conditions ($\alpha_h > 0$), circular tunnels' failure mechanism becomes asymmetrical about the vertical plane passing through the tunnel's centre. In this study, the horizontal seismic force is applied from left to right. When the horizontal earthquake acceleration coefficient $\alpha_h = 0.1$, the left horizontal failure zones from the centre of the tunnel is larger than those from the right sides, shown in Figs. 5b, 6b, 7b. When increasing $\alpha_h = 0.3$, the left horizontal failure zones are extended and larger than approximately 2-3 times those for the case $\alpha_h = 0.1$, shown in Figs. 5c, 6c, 7c.

Figs. 8a-8c show the failure mechanisms of circular tunnels with an increase in the soil weight $\gamma D/c = 2$, $\alpha_h = 0.2$ and the depth to diameter ratio of the tunnel $H/D = 1, 3, 5$. The pseudo-static seismic force is applied from left to right horizontally while the failure zones reverse the earthquake's acting. The circular tunnel's failure mechanism originates from the bottom of the tunnel and extends up to the ground surface's right sides. It means that both the horizontal earthquake acceleration coefficient α_h and the soil property $\gamma D/c$ affected a circular tunnel's failure mechanism. In these cases, the stability number becomes a negative value. It implies that normal tensile stress can be applied to the ground surface to prevent collapse, but this can not be seen in engineering practice.

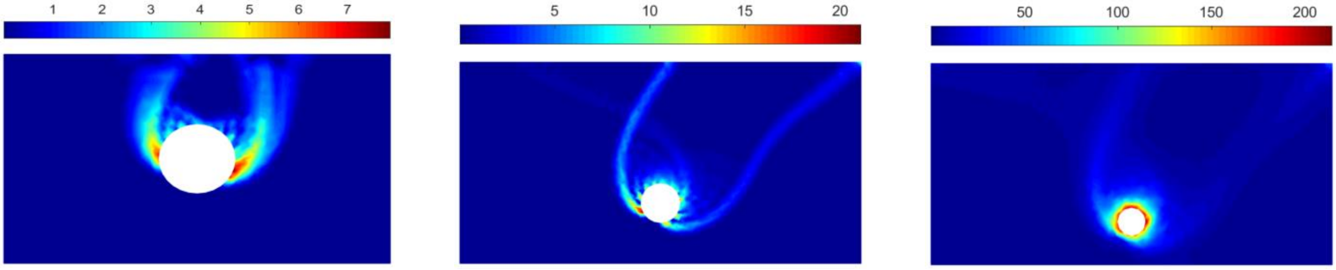

(a) H/D = 1 (b) H/D = 3 (c) H/D = 5

Fig. 8. Failure mechanism of circular tunnel for $\gamma D/c$ = 2, ϕ = 10^o, α_h = 0.2, α_v = 0

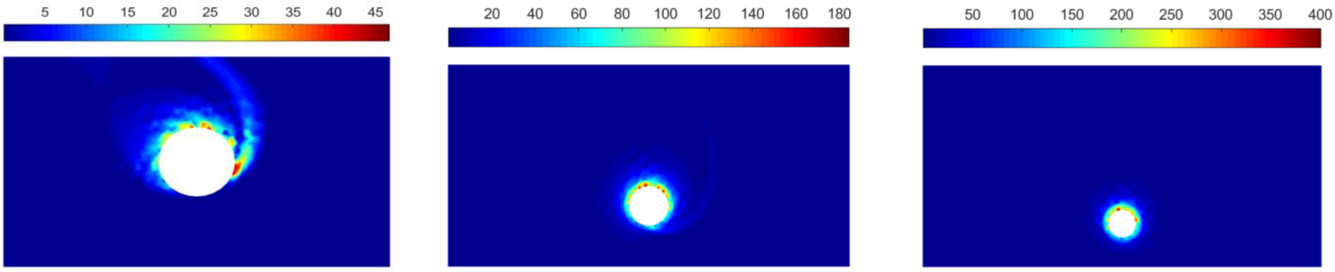

(a) H/D = 1 (b) H/D = 3 (c) H/D = 5

Fig. 9. Failure mechanism of circular tunnel for $\gamma D/c$ = 1, ϕ = 30^o, α_h = 0.1- 0.5, α_v = 0

Fig. 9a illustrates the slip surface of shallow tunnel in the case ϕ = 30^o, H/D = 1, α_h = 0.1 to 0.5 and $\gamma D/c$ = 1. It is noted that the size of the rupture zone becomes smaller with increasing values of friction angle ϕ. The failure mechanisms become around the periphery of the tunnel and do not extend to the ground surface shown in Figs. 9b, 9c in the cases H/D = 3, 5, ϕ = 30^o, α_h = 0.1 to 0.5, and $\gamma D/c$ = 1. It means that the tunnel is more stable with an increase in the soil internal friction angle ϕ, the failure zone of a circular tunnel becomes small and does not affect the ground surface.

4.2. Results of the stability numbers

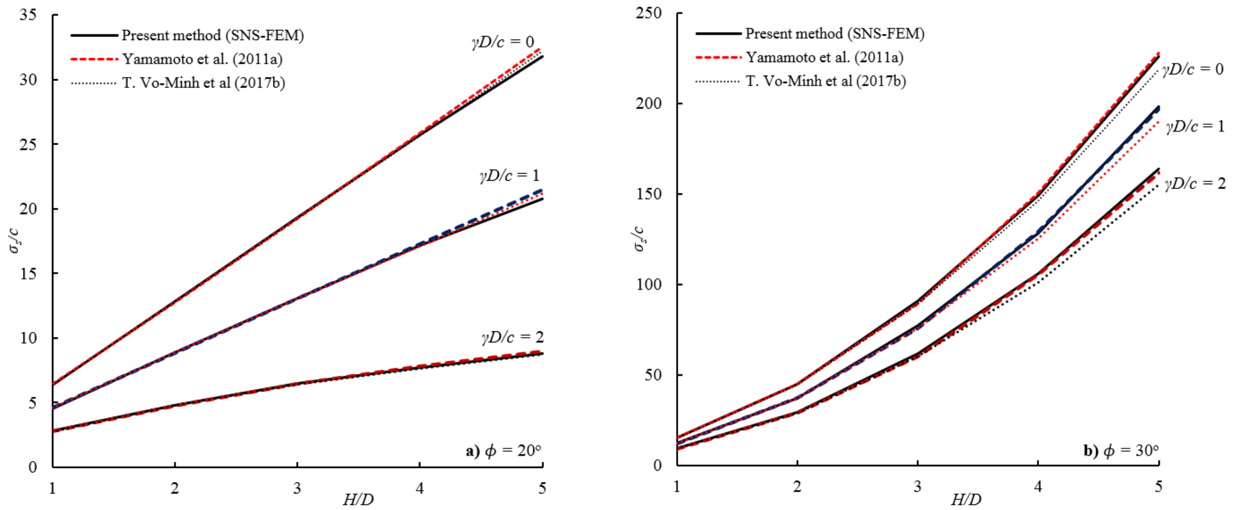

(a) ϕ = 20^o (b) ϕ = 30^o

Fig. 10. Comparisons of stability numbers of circular tunnel using SNS-FEM and other solutions:

(a) ϕ = 20^o, (b) ϕ = 30^o (smooth interface, α_h = 0, α_v = 0)

To compare the efficiency and accuracy of the present method SNS-FEM, the stability numbers of a circular tunnel under static conditions (α_h = 0) for various combinations of H/D and $\gamma D/c$ are shown in Fig. 10. The obtained results of a circular tunnel using SNS-FEM are compared with the following solutions as (1) the average values of the lower and upper bounds reported by Yamamoto et al. (2011a) using finite element limit analysis (FELA) method combined with the nonlinear programming; (2) the stability numbers investigated by T. Vo-Minh et al. (2017b) using the node-based smoothed finite element method (NS-FEM) and second-order cone programming (SOCP). The present method of SNS-FEM gives a good solution because most of the obtained results agree well with the average values of the lower and upper bounds given by Yamamoto et al. (2011a). Furthermore, this procedure used less than 4500 triangular elements (SNS-FEM) but gave a minor error compared with Yamamoto et al. (2011a) solution in which 28800 triangular elements and 43020 stress/velocity discontinuities. The errors of the stability numbers from the SNS-FEM limit analysis and the upper bound results reported by T. Vo-Minh et al. (2017b) are within ± 5%.

To show the computational efficiency of the present method, we consider the computational cost based on variables and optimization CPU times for the case H/D = 1, ϕ =10^{o}, α_h= 0.3, α_v = 0, $\gamma D/c$ = 1. The reported CPU times only refer to the time spent on the interior-point iterations for solving the resulting SOCP problem, i.e. they exclude the time taken to read the data files and execute the pre-solve routine. Results of stability numbers σ_s/c, number of variables N_{var} and CPU times between the finite element analysis using triangular elements (FEM-T3), the edge-based smoothed finite element (ES-FEM-T3) and SNS-FEM using triangular elements are summarized in Table 1.

The convergence rate archived by the present method SNS-FEM is compared with FEM-T3, ES-FEM-T3 shown in Fig. 11. With the same number of elements, the stability number values using SNS-FEM are more convergent than other existing methods such as FEM-T3 and ES-FEM-T3, although the coarse mesh is used. When the mesh is refined, the total number of SNS-FEM variables is smaller than those from FEM-T3 and ES-FEM-T3. The optimization problem using SNS-FEM is based on an interior-point algorithm with very fast convergence of about 18 - 23 step iterations with a maximum CPU time of 2.77s (N_{var} = 23750). This confirms the effectiveness of the SNS-FEM approach of using the Mosek optimizer for solving large sparse SOCP problems.

Table 1. Comparisons seismic stability numbers of a circular tunnel using SNS-FEM and other solutions (H/D = 1, ϕ =10^{o}, α_h= 0.3, α_v = 0, $\gamma D/c$ = 1, smooth interface)

N_e	FEM-T3			ES-FEM-T3			Present method SNS-FEM		
(T3)	N_{var}	CPU (s)	σ_s/c	N_{var}	CPU (s)	σ_s/c	N_{var}	CPU (s)	σ_s/c
544	2264	0.44	8.5103	3212	0.61	4.9487	1580	0.29	2.1126
818	3380	0.61	6.1521	4769	0.73	4.1928	2315	0.53	2.0975
1496	6130	0.73	5.1733	8513	1.01	3,4777	4105	0.70	2.0745
1860	7602	0.97	4.7185	10635	1.30	3.2274	5055	0.80	2.0689
2408	9818	1.19	4.1848	13709	2.66	3.0560	6485	0.89	2.0578
2844	11576	1.28	3.6841	16142	2.78	2.9475	7610	1.02	2.0498
3262	13268	1.59	3.3894	18491	3.56	2.8907	8705	1.11	2.0463
4148	16838	1.73	3.0345	23429	4.31	2.8667	10985	1.22	2.0457
5200	21076	2.43	2.8528	29290	6.05	2.7728	13690	1.45	2.0445
6728	27228	2.69	2.7520	37794	8.73	2.6803	17610	1.86	2.0432
7724	31238	3.33	2.7399	43337	9.25	2.6582	20165	2.27	2.0422
9130	36890	3.97	2.7394	51140	12.83	2.5870	23750	2.77	2.0419

N_{var}(FEM-T3) = $2N_n + 3N_e$; N_{var}(ES-FEM-T3) = $2N_n + 3N_{ed}$; N_{var}(SNS-FEM) = $5N_n$

where N_{var}, N_n, N_e and N_{ed} are the number of variables, number of nodes, number of triangular elements and number of triangular edges in the problems, respectively.

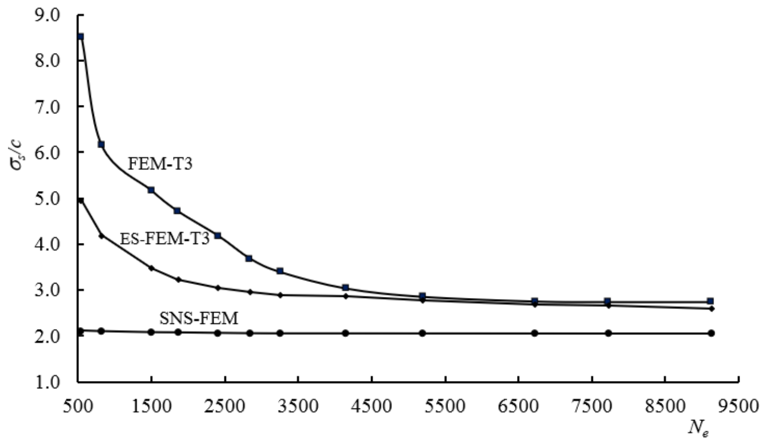

Fig. 11. The convergence rate of seismic stability numbers of a circular tunnel

$H/D = 1$, $\phi = 10^{o}$, $\alpha_h = 0.3$, $\alpha_v = 0$, $\gamma D/c = 1$

The seismic stability numbers of circular tunnels at different depths H/D varies from 1 to 5, friction angle ϕ ranges from 0^{o} to 35^{o}, and the value of α_h varies from 0 to 0.5 are listed in Table 2. Positive stability numbers signify that the tunnel collapses when subjected to compressive stress on the ground surface as per this value. In these cases, the tunnel centre's left horizontal failure mechanisms are more extensive than those from the right sides. On the other hand, the negative stability numbers imply that normal tensile stress can be applied to the ground surface to ensure no collapse occurs, but this can not be observed in engineering practice. In these cases, the horizontal seismic force acts from the left to right side, but the failure zones originate from the tunnel's bottom and extend up to the right sides of the ground surface.

In some cases of $H/D = 3$, $H/D = 5$, small friction angle $\phi < 15^{o}$ and soil properties $\gamma D/c = 1.5$ to 2, the stability numbers approximately zero are indicated by "–". It means that no surcharge loading σ_s is applied on the ground surface, and the tunnels collapse due to gravity.

Figs. 12-14 display the variation of the seismic stability numbers σ_s/c with changes in α_h and $\gamma D/c$ for a different combination of ϕ and H/D. In general, the reduction of stability numbers of circular tunnels due to the seismic degradation of the shear strength of the soil and the lateral inertia force in the soil mass. The computational results indicate that for given values of H/D and ϕ, the stability numbers decrease continuously with an increase in the horizontal earthquake acceleration coefficient α_h. For given values of H/D and $\gamma D/c$, with an increase in α_h from 0 to 0.5, the reduction in the stability number has been found approximately in a range of (i) 25%-35% for $H/D = 1$, and (ii) 30%-50% for $H/D = 3$, $H/D = 5$. In addition, the stability numbers σ_s/c for all friction angles decrease with an increase in the soil weight $\gamma D/c$, and the reduction rate tends to increase rapidly for the higher acceleration of earthquake. In contrast, the stability numbers increase continuously with an increase in the values of both H/D and ϕ.

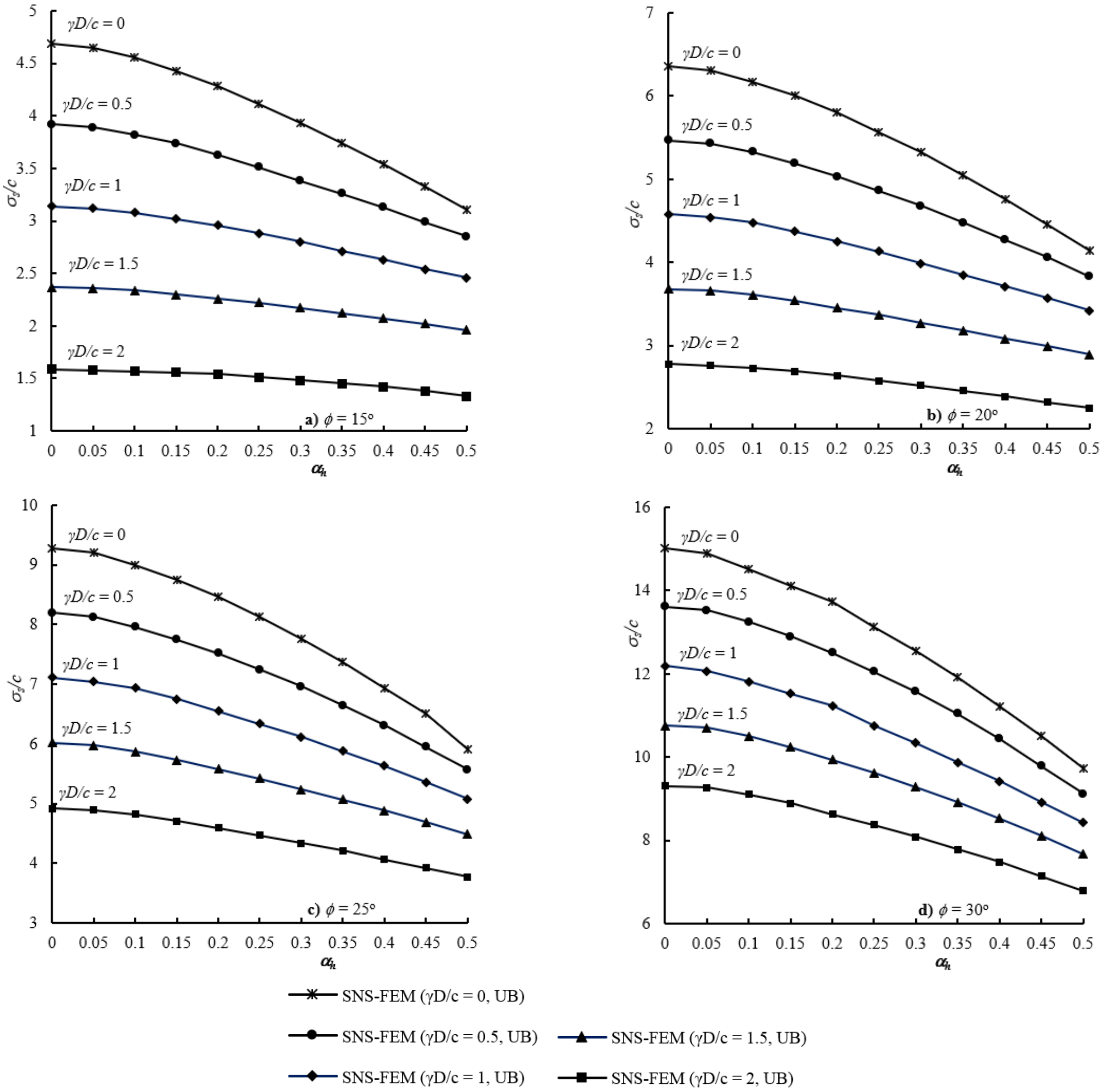

Fig. 12. Seismic stability numbers σ_s/c using the present method for the case $H/D = 1$, $\alpha_v = 0$

(a) $\phi = 15^o$, (b) $\phi = 20^o$, (c) $\phi = 25^o$, (d) $\phi = 30^o$

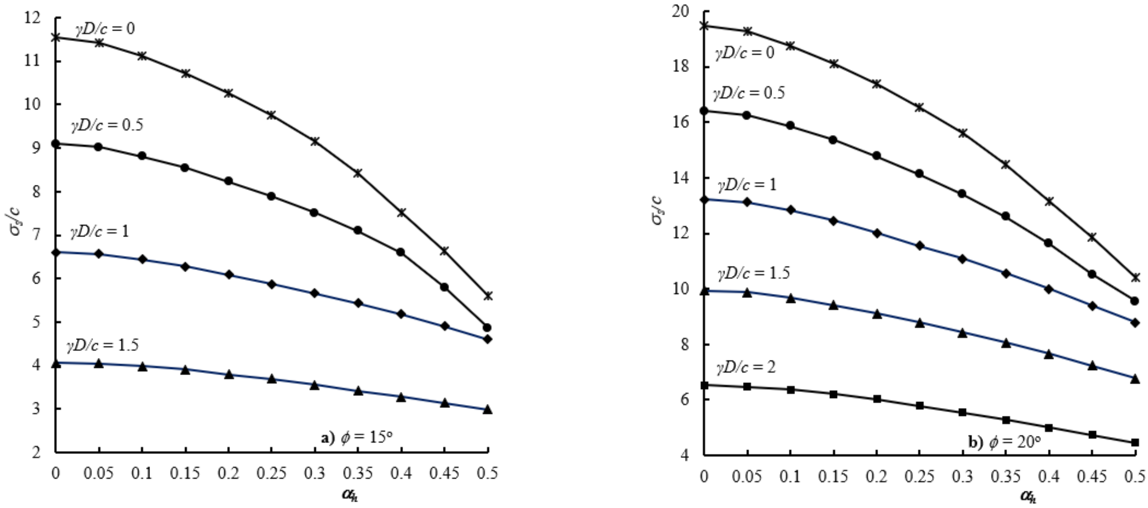

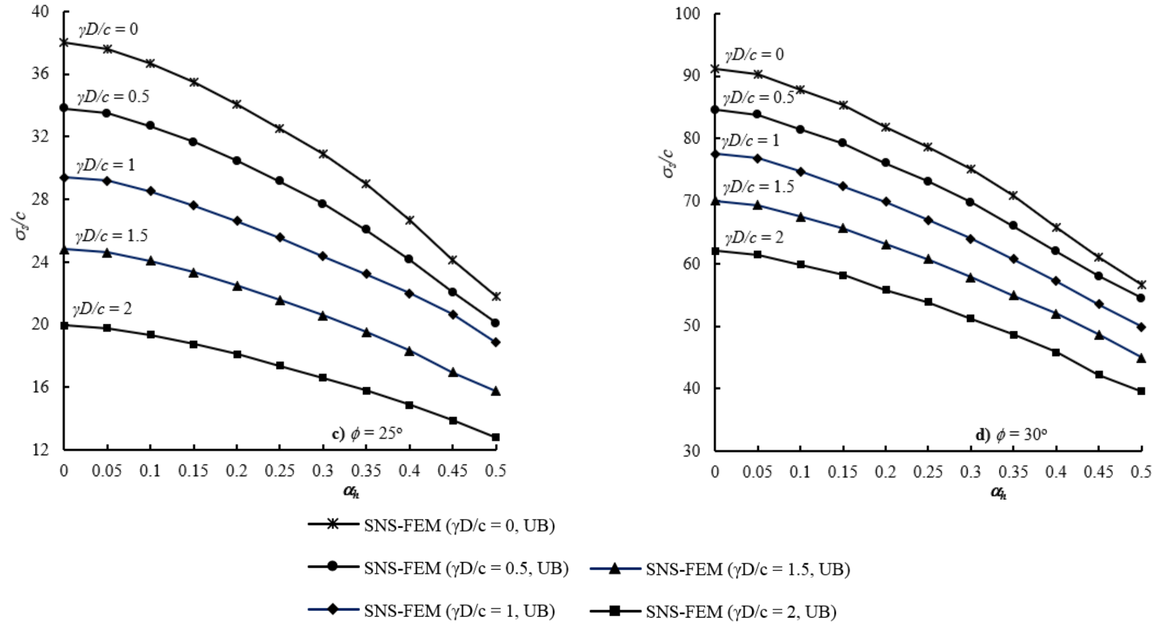

Fig. 13. Seismic stability numbers σ_s/c using the present method for the case H/D = 3, α_v = 0

(a) $\phi = 15^{\circ}$, (b) $\phi = 20^{\circ}$, (c) $\phi = 25^{\circ}$, (d) $\phi = 30^{\circ}$

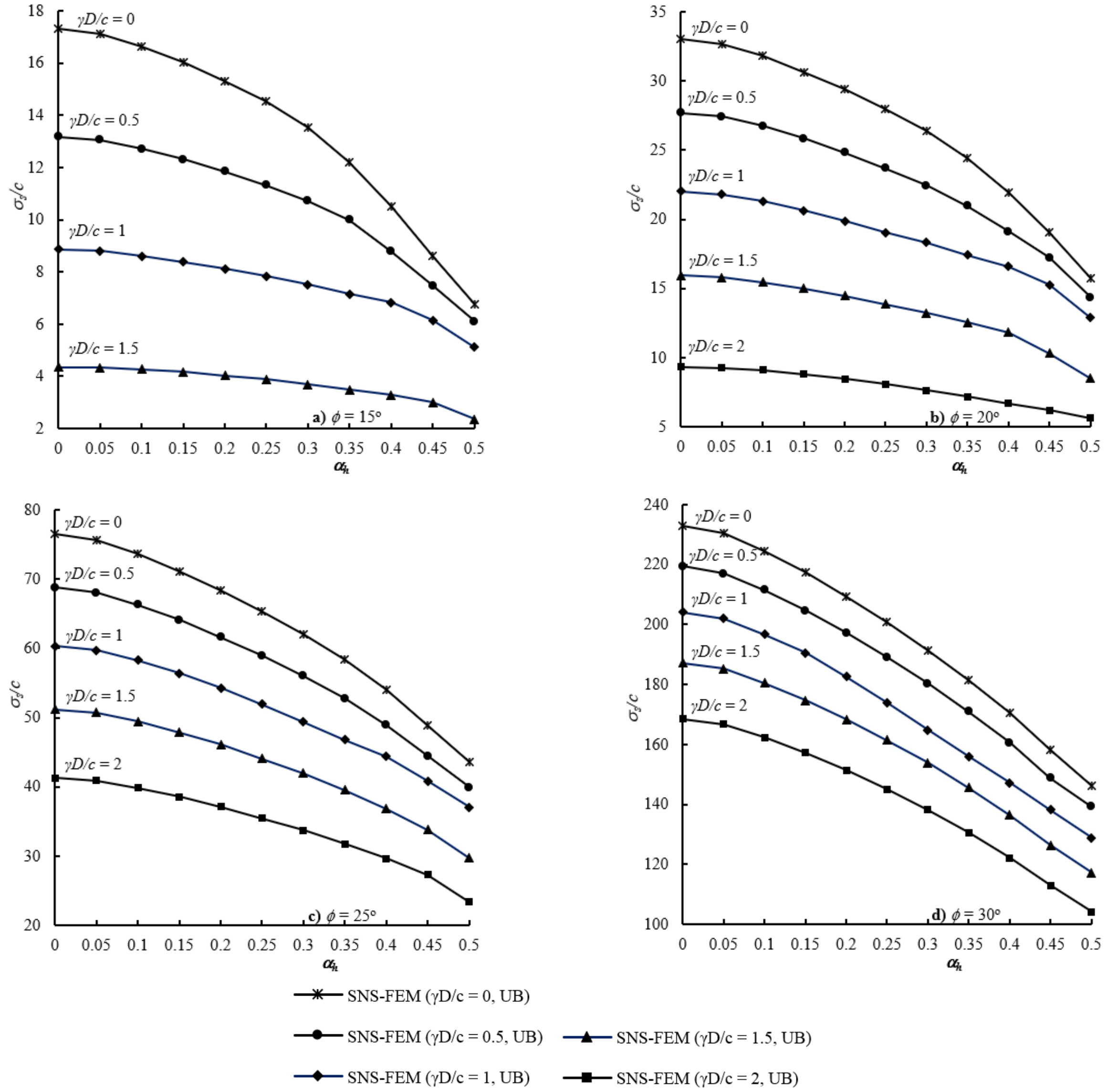

Fig. 14. Seismic stability numbers σ_s/c using the present method for the case H/D = 5, α_v = 0

(a) $\phi = 15^{\circ}$, (b) $\phi = 20^{\circ}$, (c) $\phi = 25^{\circ}$, (d) $\phi = 30^{\circ}$.

Table 2. Seismic stability numbers σ_s/c for a circular tunnel using SNS-FEM (α_v = 0)

H/D	α_h	ϕ	$\gamma D/c$					α_h	ϕ	$\gamma D/c$				
			0	0.5	1	1.5	2			0	0.5	1	1.5	2
1	0	0	2.44	1.85	1.26	0.65	0.02	0	20	6.36	5.47	4.58	3.68	2.78
	0.05		2.42	1.84	1.25	0.64	0.01	0.05		6.31	5.43	4.54	3.66	2.76
	0.10		2.37	1.82	1.24	0.63	-0.01	0.10		6.17	5.33	4.48	3.61	2.73
	0.15		2.31	1.79	1.23	0.62	-0.06	0.15		6.00	5.19	4.37	3.54	2.69
	0.20		2.24	1.75	1.22	0.61	-0.11	0.20		5.80	5.03	4.25	3.45	2.64
	0.25		2.17	1.71	1.21	0.60	-0.20	0.25		5.57	4.86	4.13	3.37	2.58
	0.30		2.08	1.67	1.19	0.59	-0.30	0.30		5.32	4.68	3.99	3.27	2.52
	0.35		2.00	1.63	1.17	0.56	-0.44	0.35		5.05	4.48	3.85	3.18	2.46
	0.40		1.92	1.58	1.15	0.53	-0.60	0.40		4.76	4.27	3.71	3.08	2.39
	0.45		1.84	1.54	1.13	0.48	-	0.45		4.46	4.06	3.57	2.99	2.32
	0.50		1.75	1.49	1.11	0.41	-	0.50		4.14	3.83	3.42	2.89	2.25
	0	5	2.94	2.31	1.67	1.04	0.38	0	25	9.28	8.20	7.11	6.02	4.92
	0.05		2.92	2.29	1.66	1.03	0.37	0.05		9.20	8.13	7.04	5.98	4.89
	0.10		2.86	2.26	1.65	1.02	0.36	0.10		9.00	7.96	6.94	5.87	4.82
	0.15		2.78	2.22	1.63	1.01	0.34	0.15		8.74	7.75	6.75	5.73	4.71
	0.20		2.69	2.17	1.61	1.00	0.31	0.20		8.46	7.52	6.55	5.58	4.59
	0.25		2.60	2.11	1.58	0.99	0.27	0.25		8.13	7.25	6.34	5.42	4.47
	0.30		2.49	2.05	1.55	0.98	0.20	0.30		7.77	6.96	6.12	5.24	4.34
	0.35		2.39	1.99	1.52	0.97	0.10	0.35		7.37	6.65	5.88	5.07	4.21
	0.40		2.28	1.93	1.49	0.95	-	0.40		6.93	6.31	5.63	4.88	4.06
	0.45		2.17	1.87	1.46	0.93	-	0.45		6.51	5.95	5.36	4.69	3.92
	0.50		2.05	1.80	1.43	0.91	-	0.50		5.91	5.57	5.08	4.49	3.77
	0	10	3.64	2.96	2.26	1.57	0.88	0	30	15.01	13.61	12.19	10.76	9.31
	0.05		3.62	2.93	2.25	1.56	0.87	0.05		14.88	13.52	12.07	10.70	9.27
	0.10		3.54	2.89	2.23	1.55	0.86	0.10		14.51	13.25	11.81	10.51	9.11
	0.15		3.44	2.83	2.20	1.54	0.85	0.15		14.12	12.90	11.53	10.24	8.89
	0.20		3.33	2.75	2.15	1.52	0.83	0.20		13.74	12.50	11.23	9.94	8.63
	0.25		3.20	2.67	2.11	1.50	0.81	0.25		13.13	12.05	10.75	9.62	8.37
	0.30		3.07	2.58	2.06	1.47	0.79	0.30		12.56	11.57	10.34	9.28	8.09
	0.35		2.93	2.50	2.01	1.44	0.76	0.35		11.93	11.04	9.88	8.92	7.79
	0.40		2.79	2.41	1.96	1.41	0.72	0.40		11.21	10.44	9.42	8.53	7.48
	0.45		2.64	2.32	1.90	1.39	0.67	0.45		10.51	9.79	8.92	8.11	7.14
	0.50		2.48	2.23	1.84	1.36	0.58	0.50		9.72	9.12	8.43	7.67	6.79
	0	15	4.69	3.92	3.14	2.37	1.59	0	35	28.27	26.24	24.17	22.07	19.94
	0.05		4.65	3.89	3.12	2.36	1.58	0.05		28.03	26.09	23.90	21.96	19.84
	0.10		4.56	3.82	3.08	2.34	1.57	0.10		27.28	25.62	23.48	21.62	19.54
	0.15		4.43	3.74	3.02	2.30	1.56	0.15		26.66	24.97	22.74	21.07	19.07
	0.20		4.28	3.63	2.96	2.26	1.54	0.20		25.85	24.20	21.95	20.44	18.51
	0.25		4.11	3.51	2.88	2.22	1.51	0.25		24.72	23.34	21.06	19.74	17.88
	0.30		3.93	3.38	2.80	2.17	1.48	0.30		23.61	22.41	20.23	18.99	17.21
	0.35		3.74	3.26	2.71	2.12	1.45	0.35		22.45	21.44	19.35	18.20	16.51
	0.40		3.54	3.13	2.63	2.07	1.42	0.40		21.07	20.31	18.41	17.33	15.75
	0.45		3.33	2.99	2.54	2.02	1.38	0.45		19.83	19.01	17.47	16.36	14.92
	0.5		3.11	2.85	2.46	1.96	1.33	0.50		18.32	17.63	16.52	15.32	14.05
3	0	0	4.13	2.47	0.80	-0.88	-2.60	0	20	19.46	16.40	13.22	9.93	6.53
	0.05		4.08	2.46	0.79	-0.92	-2.70	0.05		19.27	16.24	13.12	9.87	6.48
	0.10		3.97	2.43	0.78	-1.00	-2.87	0.10		18.77	15.86	12.84	9.68	6.38
	0.15		3.83	2.39	0.76	-1.19	-3.31	0.15		18.12	15.35	12.46	9.42	6.22
	0.20		3.65	2.33	0.73	-1.27	-4.00	0.20		17.37	14.77	12.02	9.11	6.02
	0.25		3.49	2.28	0.67	-1.76	-	0.25		16.53	14.12	11.54	8.78	5.79
	0.30		3.22	2.22	0.63	-2.33	-	0.30		15.61	13.41	11.09	8.42	5.54
	0.35		2.88	2.16	0.50	-	-	0.35		14.49	12.59	10.56	8.06	5.28

	0.40		2.52	2.10	0.47	-	-	0.40		13.16	11.63	9.99	7.66	5.01
	0.45		2.24	2.04	0.24	-	-	0.45		11.85	10.53	9.40	7.23	4.74
	0.50		2.02	1.97	0.06	-	-	0.50		10.43	9.56	8.79	6.77	4.46
	0	5	5.46	3.64	1.80	-0.03	-1.88	0	25	38.01	33.82	29.42	24.82	19.95
	0.05		5.40	3.62	1.79	-0.05	-1.95	0.05		37.62	33.51	29.19	24.62	19.78
	0.10		5.25	3.55	1.78	-0.09	-2.15	0.10		36.68	32.70	28.51	24.07	19.37
	0.15		5.06	3.47	1.76	-0.19	-2.57	0.15		35.48	31.67	27.62	23.34	18.75
	0.20		4.88	3.37	1.73	-0.32	-	0.20		34.08	30.47	26.61	22.50	18.12
	0.25		4.60	3.27	1.70	-0.57	-	0.25		32.55	29.15	25.55	21.58	17.39
	0.30		4.41	3.17	1.65	-0.71	-	0.30		30.88	27.71	24.38	20.60	16.60
	0.35		3.86	3.05	1.60	-1.81	-	0.35		28.97	26.07	23.23	19.52	15.78
	0.40		3.24	2.95	1.55	-	-	0.40		26.70	24.17	21.99	18.32	14.87
	0.45		2.80	2.78	1.49	-	-	0.45		24.15	22.08	20.65	16.97	13.89
	0.5		2.50	2.45	1.43	-	-	0.50		21.80	20.11	18.87	15.76	12.79
	0	10	7.64	5.56	3.48	1.37	-0.75	0	30	91.21	84.62	77.58	70.06	62.06
	0.05		7.56	5.53	3.46	1.36	-0.79	0.05		90.38	83.85	76.85	69.40	61.47
	0.10		7.35	5.40	3.41	1.34	-0.90	0.10		87.77	81.47	74.72	67.54	59.83
	0.15		7.08	5.26	3.35	1.31	-1.13	0.15		85.34	79.24	72.40	65.70	58.22
	0.20		6.81	5.08	3.27	1.26	-1.47	0.20		81.83	76.05	69.89	63.09	55.84
	0.25		6.44	4.90	3.19	1.20	-	0.25		78.73	73.20	67.02	60.77	53.82
	0.30		6.01	4.72	3.09	1.10	-	0.30		75.16	69.84	63.99	57.87	51.18
	0.35		5.50	4.48	3.00	0.99	-	0.35		70.90	66.03	60.71	54.91	48.63
	0.40		4.85	4.22	2.90	0.79	-	0.40		65.81	61.97	57.21	52.02	45.84
	0.45		4.12	3.81	2.80	0.44	-	0.45		61.10	58.02	53.54	48.70	42.19
	0.50		3.35	3.14	2.70	-	-	0.50		51.69	47.71	49.92	44.97	39.61
	0	15	11.54	9.10	6.61	4.06	1.46	0	35	297.38	284.08	269.57	253.76	236.67
	0.05		11.43	9.02	6.57	4.05	1.44	0.05		294.33	281.07	266.63	250.97	234.02
	0.10		11.12	8.81	6.44	3.99	1.41	0.10		287.18	274.31	259.33	245.26	228.79
	0.15		10.72	8.54	6.28	3.91	1.35	0.15		278.69	266.28	250.71	237.90	221.82
	0.20		10.26	8.23	6.09	3.80	1.26	0.20		268.90	256.99	241.90	229.69	214.14
	0.25		9.75	7.89	5.88	3.69	1.13	0.25		258.72	247.25	231.08	220.90	205.87
	0.30		9.16	7.51	5.66	3.56	0.96	0.30		247.96	237.00	220.87	211.73	197.16
	0.35		8.42	7.09	5.43	3.42	0.67	0.35		235.40	225.08	209.02	201.03	187.21
	0.40		7.53	6.59	5.18	3.28	-	0.40		221.74	211.96	197.02	189.11	175.97
	0.45		6.64	5.80	4.91	3.14	-	0.45		206.99	197.72	184.44	176.17	163.78
	0.50		5.61	4.87	4.60	2.99	-	0.50		190.93	182.36	171.86	162.29	150.74
5	0	0	5.05	2.36	-0.34	-3.06	-5.81	0	20	33.01	27.68	22.10	15.93	9.35
	0.05		4.98	2.35	-0.36	-3.18	-6.07	0.05		32.67	27.41	21.80	15.80	9.27
	0.10		4.82	2.33	-0.44	-3.47	-6.66	0.10		31.79	26.73	21.29	15.46	9.09
	0.15		4.64	2.29	-0.57	-3.93	-	0.15		30.65	25.84	20.62	14.99	8.81
	0.20		4.43	2.25	-0.74	-	-	0.20		29.38	24.83	19.86	14.46	8.48
	0.25		4.03	2.20	-0.94	-	-	0.25		27.99	23.70	19.05	13.88	8.08
	0.30		3.36	2.15	-1.32	-	-	0.30		26.42	22.44	18.33	13.24	7.65
	0.35		2.88	2.09	-	-	-	0.35		24.46	20.95	17.42	12.56	7.19
	0.40		2.52	2.04	-	-	-	0.40		21.92	19.11	16.59	11.81	6.70
	0.45		2.24	1.98	-	-	-	0.45		19.09	17.21	15.25	10.31	6.18
	0.50		2.02	1.91	-	-	-	0.50		15.76	14.37	12.89	8.52	5.65
	0.0	5	6.99	4.01	1.03	-2.00	-5.04	0.0	25	76.50	68.76	60.34	51.21	41.27
	0.05		6.92	4.00	1.02	-2.07	-	0.05		75.65	68.05	59.74	50.72	40.89
	0.10		6.70	3.91	0.97	-2.32	-	0.10		73.62	66.29	58.25	49.47	39.88
	0.15		6.44	3.84	0.94	-	-	0.15		71.14	64.10	56.36	47.88	38.58
	0.20		6.20	3.72	0.85	-	-	0.20		68.33	61.63	54.24	46.08	37.10
	0.25		5.77	3.63	0.76	-	-	0.25		65.31	58.95	51.91	44.11	35.49

0.30		4.77	3.50	0.60	-	-	0.30		62.05	56.04	49.37	41.97	33.71
0.35		3.86	3.38	0.37	-	-	0.35		58.37	52.77	46.83	39.57	31.78
0.40		3.24	3.14	0.20	-	-	0.40		54.01	48.95	44.35	36.85	29.62
0.45		2.87	2.79	-	-	-	0.45		48.82	44.42	40.84	33.77	27.27
0.50		2.53	2.45	-	-	-	0.50		43.57	39.89	37.08	29.70	23.36
0.0	10	10.46	7.04	3.54	-0.04	-3.72	0.0	30	233.03	219.46	204.15	187.19	168.47
0.05		10.34	6.97	3.52	-0.06	-3.99	0.05		230.35	217.01	201.94	185.18	166.68
0.10		10.03	6.78	3.45	-0.19	-	0.10		224.45	211.47	196.76	180.45	162.42
0.15		9.65	6.62	3.38	-0.33	-	0.15		217.35	204.74	190.48	174.71	157.23
0.20		9.25	6.36	3.30	-0.68	-	0.20		209.40	197.28	182.54	168.34	151.40
0.25		8.69	6.15	3.20	-	-	0.25		200.80	189.14	174.01	161.44	145.07
0.30		7.91	5.88	3.10	-	-	0.30		191.48	180.41	164.90	153.87	138.20
0.35		6.87	5.55	3.00	-	-	0.35		181.58	171.01	156.05	145.65	130.63
0.40		5.75	4.70	2.88	-	-	0.40		170.60	160.57	147.22	136.50	122.23
0.45		4.71	3.85	2.74	-	-	0.45		158.09	148.80	138.28	126.37	112.96
0.50		3.53	3.26	2.61	-	-	0.50		146.20	139.23	128.94	117.25	104.12
0.0	15	17.31	13.17	8.87	4.36	-0.38	0.0	35	1066.9	1032.1	992.48	948.07	897.34
0.05		17.11	13.05	8.80	4.33	-0.44	0.05		1053.0	1019.1	980.08	936.07	886.75
0.10		16.63	12.72	8.60	4.27	-0.62	0.10		1027.4	994.36	956.26	913.70	865.29
0.15		16.01	12.31	8.39	4.16	-0.99	0.15		996.21	963.88	923.72	884.95	838.04
0.20		15.31	11.84	8.12	4.03	-	0.20		963.07	931.84	879.89	834.99	789.36
0.25		14.53	11.32	7.83	3.88	-	0.25		926.63	896.25	835.49	790.12	740.71
0.30		13.53	10.72	7.51	3.69	-	0.30		888.54	859.21	791.48	747.32	702.51
0.35		12.18	9.99	7.16	3.49	-	0.35		845.90	817.80	750.44	710.66	667.02
0.40		10.50	8.78	6.82	3.28	-	0.40		801.30	774.26	703.01	670.47	626.94
0.45		8.63	7.48	6.15	3.00	-	0.45		751.75	726.09	661.26	632.05	591.30
0.50		6.77	6.10	5.11	2.36	-	0.50		699.68	675.02	616.50	589.91	551.97

To quantify the effect of the earthquake on a circular tunnel's stability results, corrective coefficients e_{sE} that are defined as the ratios of the seismic stability to its static counterpart are computed. Table 3 presents the variation of the corrective coefficients e_{sE} with the horizontal earthquake acceleration coefficient α_h in the case $\phi = 20^o$ and $\phi = 35^o$, $\gamma D/c = 0$ and $\gamma D/c = 1$.

Table 3. Corrective coefficients to account for soil inertia effect of circular tunnels using SNS-FEM

$\gamma D/c$	α_h	σ_s/c						e_{sE}					
		H/D = 1		H/D = 3		H/D = 5		H/D = 1		H/D = 3		H/D = 5	
	ϕ	20°	35°	20°	35°	20°	35°	20°	35°	20°	35°	20°	35°
0	0	6.36	28.27	19.46	297.38	33.01	1066.9	1	1	1	1	1	1
	0.05	6.31	28.03	19.27	294.33	32.67	1053.0	0.9921	0.9915	0.9902	0.9897	0.9897	0.9870
	0.10	6.17	27.28	18.77	287.18	31.79	1027.4	0.9701	0.9650	0.9645	0.9657	0.9630	0.9630
	0.15	6.00	26.66	18.12	278.69	30.65	996.21	0.9434	0.9430	0.9311	0.9372	0.9285	0.9337
	0.20	5.80	25.85	17.37	268.90	29.38	963.07	0.9119	0.9144	0.8926	0.9042	0.8900	0.9027
	0.25	5.57	24.72	16.53	258.72	27.99	926.63	0.8758	0.8744	0.8494	0.8700	0.8479	0.8685
	0.30	5.32	23.61	15.61	247.96	26.42	888.54	0.8365	0.8352	0.8022	0.8338	0.8004	0.8328
	0.35	5.05	22.45	14.49	235.40	24.46	845.90	0.7940	0.7941	0.7446	0.7916	0.7410	0.7929
	0.40	4.76	21.07	13.16	221.74	21.92	801.30	0.7484	0.7453	0.6763	0.7456	0.6640	0.7511
	0.45	4.46	19.83	11.85	206.99	19.09	751.75	0.7013	0.7015	0.6089	0.6960	0.5783	0.7046
	0.50	4.14	18.32	10.43	190.93	15.76	699.68	0.6509	0.6480	0.5360	0.6420	0.4774	0.6558
1	0	4.58	24.17	13.22	269.57	22.01	992.48	1	1	1	1	1	1
	0.05	4.54	23.90	13.12	266.63	21.80	980.08	0.9913	0.9888	0.9924	0.9891	0.99046	0.98751
	0.10	4.48	23.48	12.84	259.33	21.29	956.26	0.9782	0.9715	0.9713	0.9620	0.96729	0.96351
	0.15	4.37	22.74	12.46	250.71	20.62	923.72	0.9541	0.9408	0.9425	0.9300	0.93685	0.93072

0.20	4.25	21.95	12.02	241.90	19.86	879.89	0.9279	0.9082	0.9092	0.8974	0.90232	0.88656
0.25	4.13	21.06	11.54	231.08	19.05	835.49	0.9017	0.8713	0.8729	0.8572	0.87006	0.84182
0.30	3.99	20.23	11.09	220.87	18.33	791.48	0.8712	0.8370	0.8389	0.8193	0.83280	0.79748
0.35	3.85	19.35	10.56	209.02	17.42	750.44	0.8406	0.8006	0.7988	0.7754	0.79146	0.75613
0.40	3.71	18.41	9.99	197.02	16.59	703.01	0.8100	0.7617	0.7557	0.7309	0.75375	0.70834
0.45	3.57	17.47	9.40	184.44	15.25	661.26	0.7795	0.7228	0.7110	0.6842	0.71104	0.66627
0.50	3.42	16.52	8.79	171.86	12.89	616.50	0.7467	0.6835	0.6649	0.6375	0.66742	0.62117

For weightless soil $\gamma D/c = 0$, the curves obtained for e_{sE} are plotted in Fig. 15 for the case $H/D = 1, 3, 5$ and show that the cohesion significantly affects the stability numbers of a circular tunnel. In the cases medium and deep tunnels, the coefficients e_{sE} are noticeably affected by both α_h and ϕ (Figs. 15b-15c), whereas the coefficients e_{sE} (Fig. 15a) in case shallow tunnel decrease for increasing α_h, but is less influenced by the angle ϕ. For example, when $\alpha_h = 0.5$, $\alpha_v = 0$, $H/D = 1$, $\phi = 20^o$ and $\phi = 35^o$, the corrective coefficients are the same such as $e_{sE} = 0.651$ and $e_{sE} = 0.648$. In contrast, when $H/D = 3$, $\alpha_h = 0.5$, the corrective coefficients are different as $e_{sE} = 0.536$, $e_{sE} = 0.642$ in the cases $\phi = 20^o$ and $\phi = 35^o$, respectively.

Fig. 16 demonstrates the variation of the corrective coefficients e_{sE} with the horizontal earthquake acceleration coefficient α_h for the case $H/D = 1, 3, 5$ and $\gamma D/c = 1$. It is evident that soil inertia significantly affects the stability numbers of a circular tunnel. The corrective coefficients for all friction angles decrease with an increase in α_h and the reduction rate tends to increase rapidly for the higher acceleration of earthquake. For example, when $\alpha_h = 0.3$, $\alpha_v = 0$, $\phi = 20^o$ and $\gamma D/c = 1$, the corrective coefficients are small changes $e_{sE} = 0.871$, $e_{sE} = 0.838$, $e_{sE} = 0.832$ in the cases $H/D = 1, 3, 5$, respectively. In contrast, when $\alpha_h = 0.5$, the corrective coefficients reduce to $e_{sE} = 0.746$, $e_{sE} = 0.664$, $e_{sE} = 0.667$ in the cases $H/D = 1, 3, 5$, respectively.

Fig. 15 shows that for given values of H/D and $\alpha_h > 0.25$, increasing the internal angle of soil ϕ, the reduction rate of the corrective coefficients tends to decrease. In contrast, the reduction rate of the corrective coefficients tends to increase with an increase in the internal angle of soil ϕ, shown in Fig. 16. Different from the tendency shown in Fig. 15 and Fig. 16 due to the effect of the lateral inertia force in the soil mass to reduce the corrective coefficients of circular tunnels.

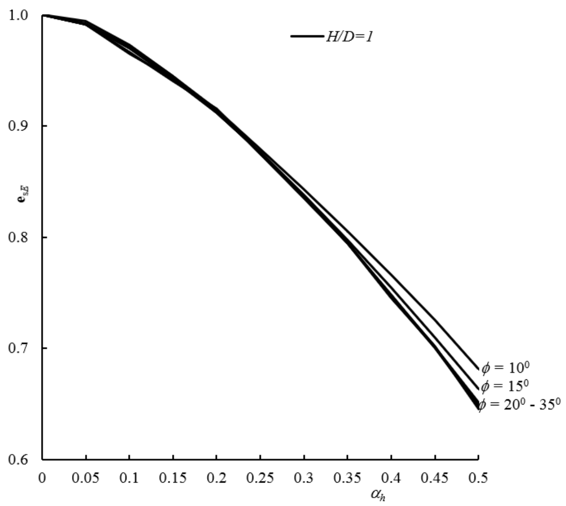

(a) $H/D = 1$, $\gamma D/c = 0$

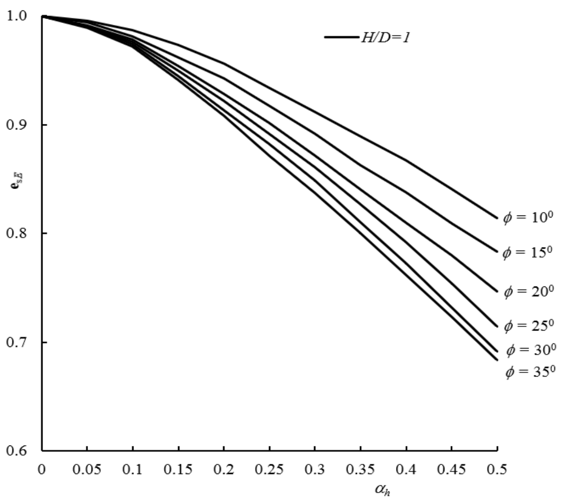

(a) $H/D = 1$, $\gamma D/c = 1$

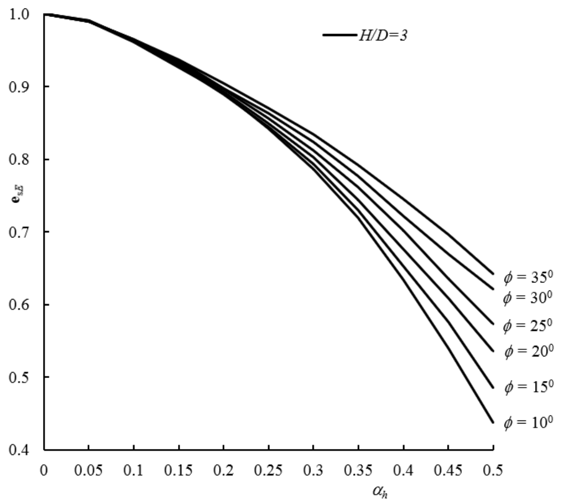

(b) H/D = 3, $\gamma D/c$ = 0

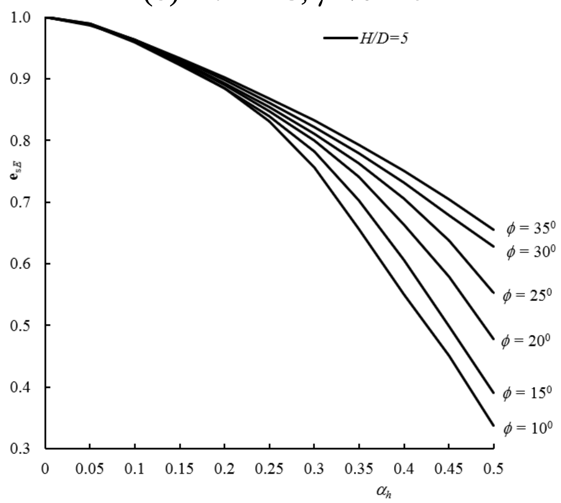

(c) H/D = 5, $\gamma D/c$ = 0

Fig. 15. Corrective coefficients to account for cohesion of soil effect on stability of circular tunnels (a) H/D = 1, (b) H/D = 3, (c) H/D = 5

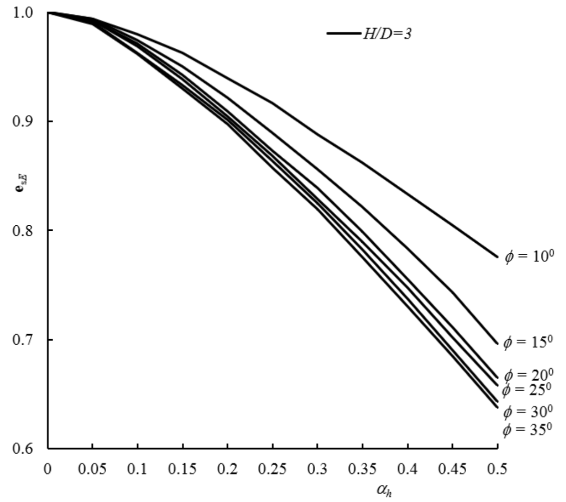

(b) H/D = 3, $\gamma D/c$ = 1

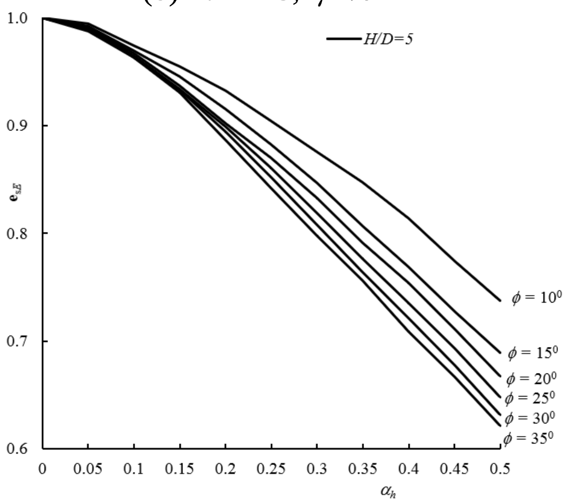

(c) H/D = 5, $\gamma D/c$ = 1

Fig. 16. Corrective coefficients to account for soil inertia effect on stability of circular tunnels (a) H/D = 1, (b) H/D = 3, (c) H/D = 5

4.3. Effect of the vertical acceleration α_v on the stability numbers σ_s/c

To consider the effect of horizontal and vertical acceleration on the stability of a circular tunnel, the ratio α_v/α_h from -1 to 1 is investigated. In this paper, the horizontal earthquake acceleration coefficient α_h varies from 0 to 0.5, the soil properties $\gamma D/c$ range from 0.5 to 2, and the values of friction angle ϕ = 20° and ϕ =30° are considered. In the presence of the combination α_v and α_h, the soil mass is subjected to the body force per unit volume in the vertical downward $(1-\alpha_v)\gamma$ and the horizontal directions $\alpha_h\gamma$. The vertical surcharge $(1-\alpha_v)\sigma_s$ and the horizontal surcharge loadings $\alpha_h\sigma_s$ are applied to the ground surface.

Table 4 summarizes the stability numbers σ_s/c to consider the effect of both horizontal and vertical components of the seismic acceleration for the cases $\phi = 20^o$, $\phi = 30^o$. Corrective coefficients e_{sE} were defined as the ratios of seismic to static surcharge loadings to point out the reduction in stability of circular tunnels due to seismic effects. A comparison of the effect of the ratio α_v/α_h on the corrective coefficient e_{sE} is shown in Figs. 17-19 for $\phi = 20^o$, $\phi = 30^o$ and H/D = 1, 3, 5. It can be observed that negative values of α_v (downward acceleration) increase the inclination of soil inertia and surcharge loading; therefore, the factors e_{sE} decrease with increasing in α_h and it reduces the stability of circular tunnels, geotechnical engineers need to consider this problem in the seismic preliminary design stage of circular tunnels. In contrast, positive values of α_v (upward acceleration), $\alpha_h \leq 0.25$, $\alpha_v/\alpha_h = 0.5$ and $\alpha_v/\alpha_h = 1$, it reduces the vertical component of the surcharge and soil inertia. Therefore, the factors e_{sE} increase with α_h, indicating that it increases the stability of circular tunnels and the corrective coefficient e_{sE} gains the maximum value when $\alpha_h = 0.25$. For example, when $\alpha_h = 0.25$, $\alpha_v/\alpha_h = 1$, $\phi = 20^o$ and $\gamma D/c = 1$, the corrective coefficients are maximum values $e_{sE} = 1.22$, $e_{sE} = 1.19$, $e_{sE} = 1.18$ in the cases H/D = 1, 3, 5, respectively. In the case $\alpha_h > 0.25$, the factors e_{sE} decrease and dropdown zero when $\alpha_h = 0.35$ (in case $\alpha_v/\alpha_h = 1$, H/D = 3 and 5) and $\alpha_h = 0.4$ (in case $\alpha_v/\alpha_h = 0.5$, H/D = 3 and 5).

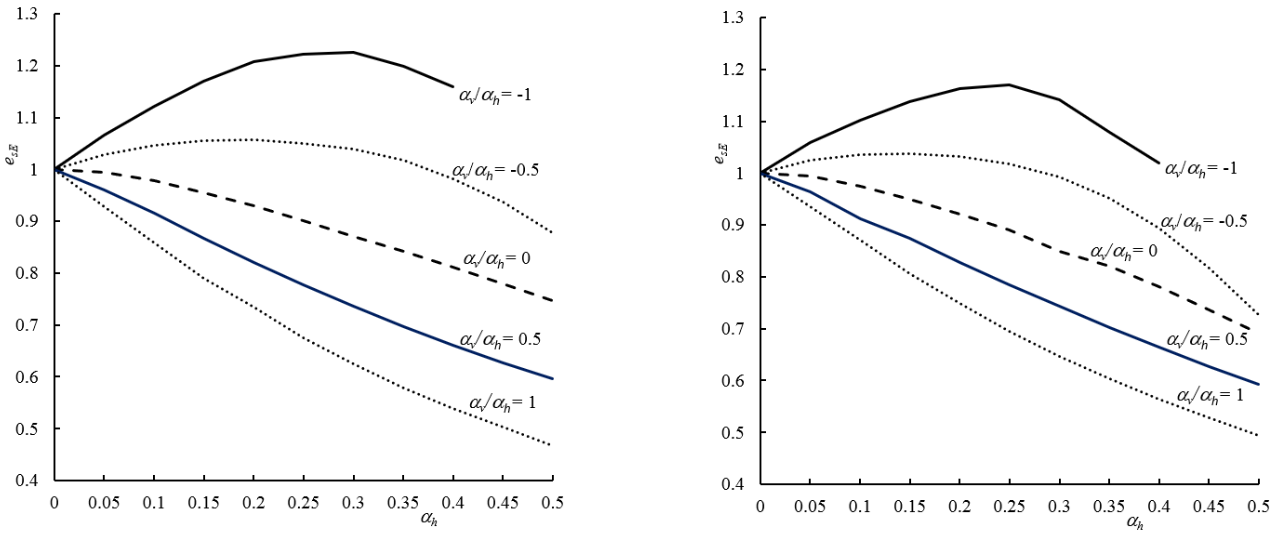

(a) $H/D = 1$, $\gamma D/c = 1$, $\phi = 20^o$ (b) $H/D = 1$, $\gamma D/c = 1$, $\phi = 30^o$

Fig. 17. Corrective coefficients to account for effect of vertical acceleration α_v on stability of circular tunnels for the case $H/D = 1$: (a) $\phi = 20^o$, (b) $\phi = 30^o$

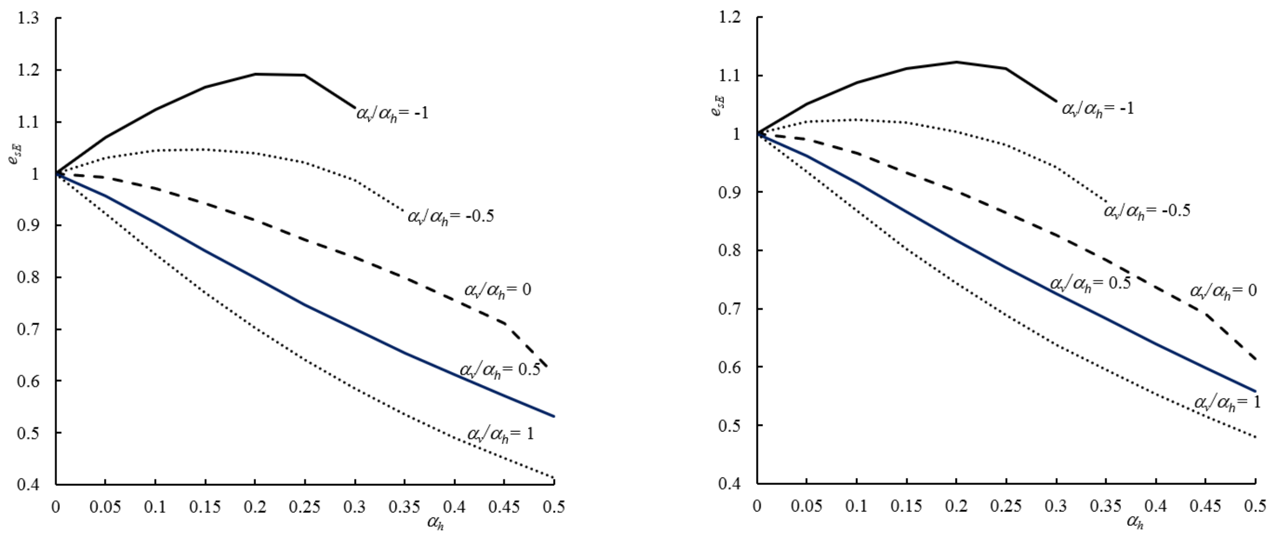

(a) $H/D = 3$, $\gamma D/c = 1$, $\phi = 20^o$ (b) $H/D = 3$, $\gamma D/c = 1$, $\phi = 30^o$

Fig. 18. Corrective coefficients to account for effect of vertical acceleration α_v on stability of circular tunnels for the case $H/D = 3$: (a) $\phi = 20^o$, (b) $\phi = 30^o$

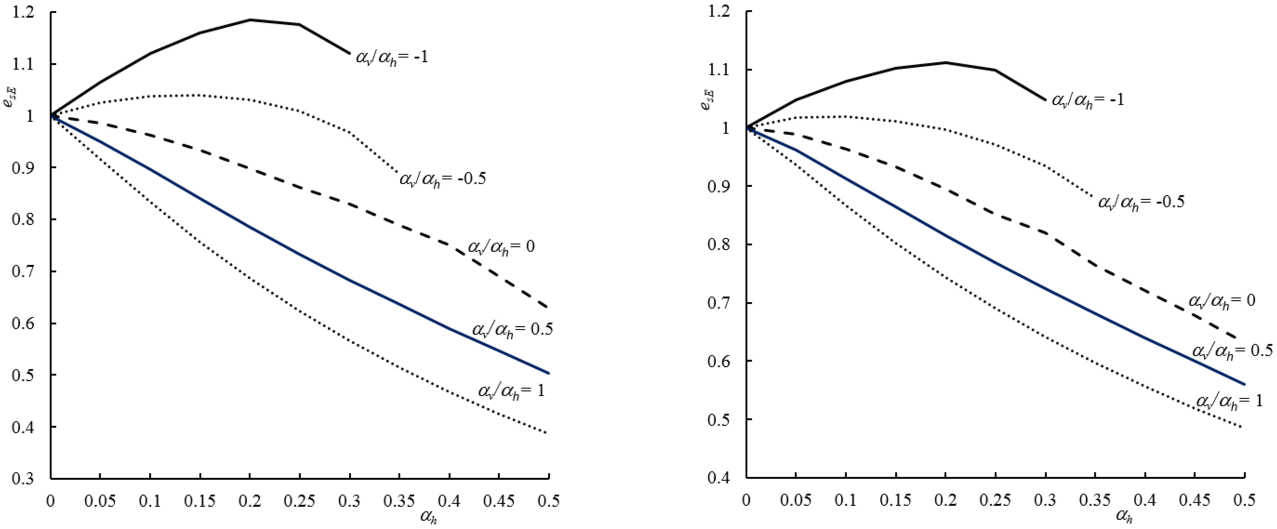

(a) H/D = 5, $\gamma D/c$ = 1, ϕ = 20^o (b) H/D = 5, $\gamma D/c$ = 1, ϕ = 30^o

Fig. 19. Corrective coefficients to account for effect of vertical acceleration α_v on stability of circular tunnels for the case H/D = 5: (a) ϕ = 20^o, (b) ϕ = 30^o

Table 4. Seismic stability numbers σ_s/c for a circular tunnel using SNS-FEM ($\alpha_v \neq 0$)

H/D	α_h	α_v	ϕ = 20^o				α_h	α_v	ϕ =30^o			
			$\gamma D/c$						$\gamma D/c$			
			0.5	1	1.5	2			0.5	1	1.5	2
1	0	0	5.47	4.58	3.68	2.78	0	0	13.61	12.19	10.76	9.31
	0.05	α_v= -α_h	5.76	4.88	3.99	3.10	0.05	α_v= -α_h	14.29	12.90	11.49	10.06
		α_v= -0.5α_h	5.59	4.71	3.82	2.93		α_v= -0.5α_h	13.90	12.50	11.09	9.66
		α_v= 0	5.47	4.55	3.66	2.76		α_v= 0	13.52	12.12	10.70	9.27
		α_v= 0.5α_h	5.28	4.40	3.51	2.61		α_v= 0.5α_h	13.16	11.76	10.34	8.91
		α_v= α_h	5.14	4.25	3.36	2.47		α_v= α_h	12.82	11.41	9.99	8.56
	0.10	α_v= -α_h	5.99	5.14	4.28	3.42	0.10	α_v= -α_h	14.79	13.44	12.08	10.70
		α_v= -0.5α_h	5.64	4.79	3.93	3.06		α_v= -0.5α_h	13.98	12.63	11.26	9.87
		α_v= 0	5.33	4.48	3.61	2.74		α_v= 0	13.25	11.89	10.51	9.11
		α_v= 0.5α_h	5.05	4.19	3.32	2.44		α_v= 0.5α_h	12.58	11.22	9.84	8.43
		α_v= α_h	4.79	3.93	3.05	2.17		α_v= α_h	11.98	10.61	9.22	7.81
	0.15	α_v= -α_h	6.16	5.36	4.55	3.73	0.15	α_v= -α_h	15.16	13.87	12.57	11.25
		α_v= -0.5α_h	5.64	4.83	4.01	3.17		α_v= -0.5α_h	13.95	12.64	11.32	9.98
		α_v= 0	5.19	4.37	3.54	2.69		α_v= 0	12.90	11.58	10.24	8.89
		α_v= 0.5α_h	4.80	3.97	3.13	2.27		α_v= 0.5α_h	11.98	10.65	9.30	7.93
		α_v= α_h	4.46	3.62	2.77	1.90		α_v= α_h	11.17	9.83	8.47	7.09
	0.20	α_v= -α_h	6.26	5.53	4.79	4.02	0.20	α_v= -α_h	15.37	14.17	12.96	11.72
		α_v= -0.5α_h	5.60	4.84	4.06	3.26		α_v= -0.5α_h	13.81	12.57	11.32	10.04
		α_v= 0	5.04	4.26	3.46	2.64		α_v= 0	12.50	11.23	9.94	8.63
		α_v= 0.5α_h	4.56	3.76	2.95	2.11		α_v= 0.5α_h	11.38	10.09	8.78	7.45
		α_v= α_h	4.15	3.34	2.51	1.66		α_v= α_h	10.42	9.12	7.79	6.43
	0.25	α_v= -α_h	6.27	5.65	4.98	4.29	0.25	α_v= -α_h	15.32	14.26	13.18	12.07
		α_v= -0.5α_h	5.51	4.81	4.09	3.34		α_v= -0.5α_h	13.55	12.41	11.24	10.04
		α_v= 0	4.86	4.13	3.37	2.58		α_v= 0	12.05	10.85	9.62	8.37
		α_v= 0.5α_h	4.33	3.56	2.77	1.96		α_v= 0.5α_h	10.80	9.56	8.29	6.99
		α_v= α_h	3.88	3.09	2.28	1.44		α_v= α_h	9.75	8.47	7.17	5.84
	0.30	α_v= -α_h	6.14	5.65	5.11	4.51	0.30	α_v= -α_h	14.75	13.91	13.03	12.12
		α_v= -0.5α_h	5.37	4.76	4.10	3.41		α_v= -0.5α_h	13.13	12.11	11.05	9.95
		α_v= 0	4.68	3.99	3.28	2.52		α_v= 0	11.57	10.34	9.28	8.09
		α_v= 0.5α_h	4.10	3.37	2.61	1.81		α_v= 0.5α_h	10.24	9.05	7.82	6.56
		α_v= α_h	3.62	2.86	2.07	1.23		α_v= α_h	9.13	7.89	6.62	5.31
	0.35	α_v= -α_h	5.78	5.49	5.12	4.67	0.35	α_v= -α_h	13.46	12.94	12.34	11.69
		α_v= -0.5α_h	5.16	4.66	4.08	3.45		α_v= -0.5α_h	12.46	11.60	10.70	9.75

		$\alpha_v = 0$	4.48	3.86	3.18	2.46		$\alpha_v = 0$	11.04	10.01	8.92	7.79
		$\alpha_v = 0.5\alpha_h$	3.89	3.19	2.46	1.67		$\alpha_v = 0.5\alpha_h$	9.70	8.56	7.38	6.16
		$\alpha_v = \alpha_h$	3.39	2.65	1.88	1.03		$\alpha_v = \alpha_h$	8.56	7.36	6.12	4.82
	0.40	$\alpha_v = -\alpha_h$	5.19	5.11	4.92	4.65	0.40	$\alpha_v = -\alpha_h$	-	11.20	10.93	10.59
		$\alpha_v = -0.5\alpha_h$	4.89	4.50	4.03	3.47		$\alpha_v = -0.5\alpha_h$	11.56	10.90	10.18	9.39
		$\alpha_v = 0$	4.28	3.72	3.08	2.39		$\alpha_v = 0$	10.44	9.51	8.53	7.48
		$\alpha_v = 0.5\alpha_h$	3.69	3.03	2.32	1.54		$\alpha_v = 0.5\alpha_h$	9.18	8.10	6.97	5.77
		$\alpha_v = \alpha_h$	3.18	2.47	1.70	0.85		$\alpha_v = \alpha_h$	8.04	6.87	5.66	4.37
	0.45	$\alpha_v = -\alpha_h$	-	-	-	-	0.45	$\alpha_v = -\alpha_h$	-	-	-	-
		$\alpha_v = -0.5\alpha_h$	4.54	4.29	3.94	3.46		$\alpha_v = -0.5\alpha_h$	10.39	9.96	9.44	8.82
		$\alpha_v = 0$	4.06	3.57	2.99	2.32		$\alpha_v = 0$	9.79	8.98	8.11	7.14
		$\alpha_v = 0.5\alpha_h$	3.50	2.87	2.19	1.41		$\alpha_v = 0.5\alpha_h$	8.67	7.65	6.58	5.40
		$\alpha_v = \alpha_h$	2.99	2.30	1.54	0.67		$\alpha_v = \alpha_h$	7.57	6.44	5.24	3.97
	0.50	$\alpha_v = -\alpha_h$	-	-	-	-	0.50	$\alpha_v = -\alpha_h$	-	-	-	-
		$\alpha_v = -0.5\alpha_h$	4.15	4.02	3.78	3.42		$\alpha_v = -0.5\alpha_h$	-	8.86	8.55	8.14
		$\alpha_v = 0$	3.83	3.42	2.89	2.25		$\alpha_v = 0$	9.12	8.43	7.67	6.79
		$\alpha_v = 0.5\alpha_h$	3.32	2.73	2.06	1.29		$\alpha_v = 0.5\alpha_h$	8.17	7.23	6.21	5.06
		$\alpha_v = \alpha_h$	2.82	2.14	1.39	0.48		$\alpha_v = \alpha_h$	7.13	6.03	4.86	3.59
3	0	0	16.40	13.22	9.93	6.53	0	0	84.62	77.58	70.06	62.06
	0.05	$\alpha_v = -\alpha_h$	17.26	14.14	10.91	7.55	0.05	$\alpha_v = -\alpha_h$	88.54	81.57	74.18	66.36
		$\alpha_v = -0.5\alpha_h$	16.74	13.62	10.38	7.00		$\alpha_v = -0.5\alpha_h$	86.14	79.15	71.73	63.85
		$\alpha_v = 0$	16.25	13.12	9.87	6.48		$\alpha_v = 0$	83.85	76.85	69.40	61.47
		$\alpha_v = 0.5\alpha_h$	15.79	12.65	9.39	5.99		$\alpha_v = 0.5\alpha_h$	81.68	74.66	67.18	59.20
		$\alpha_v = \alpha_h$	15.35	12.20	8.93	5.52		$\alpha_v = \alpha_h$	79.61	72.56	65.05	57.02
	0.10	$\alpha_v = -\alpha_h$	17.84	14.86	11.76	8.54	0.10	$\alpha_v = -\alpha_h$	91.07	84.39	77.30	69.79
		$\alpha_v = -0.5\alpha_h$	16.80	13.80	10.68	7.41		$\alpha_v = -0.5\alpha_h$	86.23	79.49	72.32	64.71
		$\alpha_v = 0$	15.86	12.84	9.68	6.38		$\alpha_v = 0$	81.47	75.04	67.54	59.83
		$\alpha_v = 0.5\alpha_h$	15.01	11.96	8.78	5.44		$\alpha_v = 0.5\alpha_h$	77.83	70.98	63.65	55.84
		$\alpha_v = \alpha_h$	14.23	11.16	7.95	4.57		$\alpha_v = \alpha_h$	74.16	67.26	59.86	51.94
	0.15	$\alpha_v = -\alpha_h$	18.20	15.41	12.49	9.44	0.15	$\alpha_v = -\alpha_h$	92.57	86.28	79.59	72.50
		$\alpha_v = -0.5\alpha_h$	16.68	13.83	10.85	7.73		$\alpha_v = -0.5\alpha_h$	85.45	79.03	72.18	64.90
		$\alpha_v = 0$	15.35	12.46	9.42	6.22		$\alpha_v = 0$	79.24	72.40	65.70	58.22
		$\alpha_v = 0.5\alpha_h$	14.19	11.25	8.16	4.88		$\alpha_v = 0.5\alpha_h$	73.81	67.15	60.01	52.34
		$\alpha_v = \alpha_h$	13.16	10.18	7.04	3.68		$\alpha_v = \alpha_h$	68.99	62.23	54.95	47.10
	0.20	$\alpha_v = -\alpha_h$	18.27	15.75	13.08	10.26	0.20	$\alpha_v = -\alpha_h$	92.93	87.09	80.88	74.28
		$\alpha_v = -0.5\alpha_h$	16.39	13.74	10.94	7.96		$\alpha_v = -0.5\alpha_h$	83.94	77.86	71.37	64.45
		$\alpha_v = 0$	14.77	12.02	9.11	6.02		$\alpha_v = 0$	76.05	69.89	63.09	55.84
		$\alpha_v = 0.5\alpha_h$	13.38	10.55	7.56	4.34		$\alpha_v = 0.5\alpha_h$	69.85	63.41	56.46	48.95
		$\alpha_v = \alpha_h$	12.17	9.28	6.20	2.86		$\alpha_v = \alpha_h$	64.22	57.64	50.49	42.72
	0.25	$\alpha_v = -\alpha_h$	17.87	15.73	13.43	10.91	0.25	$\alpha_v = -\alpha_h$	91.51	86.23	80.62	74.64
		$\alpha_v = -0.5\alpha_h$	15.90	13.50	10.92	8.13		$\alpha_v = -0.5\alpha_h$	81.76	76.07	69.97	63.45
		$\alpha_v = 0$	14.12	11.54	8.78	5.79		$\alpha_v = 0$	73.20	67.02	60.77	53.82
		$\alpha_v = 0.5\alpha_h$	12.59	9.88	6.98	3.81		$\alpha_v = 0.5\alpha_h$	65.96	59.73	52.98	45.65
		$\alpha_v = \alpha_h$	11.28	8.47	5.45	2.07		$\alpha_v = \alpha_h$	59.86	53.41	46.37	38.66
	0.30	$\alpha_v = -\alpha_h$	16.34	14.90	13.21	11.24	0.30	$\alpha_v = -\alpha_h$	86.37	81.88	77.09	71.96
		$\alpha_v = -0.5\alpha_h$	15.10	13.04	10.77	8.21		$\alpha_v = -0.5\alpha_h$	78.30	73.10	67.51	61.51
		$\alpha_v = 0$	13.41	11.09	8.42	5.54		$\alpha_v = 0$	69.84	64.16	57.87	51.18
		$\alpha_v = 0.5\alpha_h$	11.83	9.25	6.44	3.29		$\alpha_v = 0.5\alpha_h$	62.31	56.28	49.70	42.53
		$\alpha_v = \alpha_h$	10.46	7.74	4.77	1.32		$\alpha_v = \alpha_h$	55.87	49.57	42.65	35.01
	0.35	$\alpha_v = -\alpha_h$	-	-	-	-	0.35	$\alpha_v = -\alpha_h$	-	-	-	-
		$\alpha_v = -0.5\alpha_h$	13.79	12.24	10.40	8.18		$\alpha_v = -0.5\alpha_h$	73.13	68.52	63.55	58.18
		$\alpha_v = 0$	12.59	10.56	8.06	5.28		$\alpha_v = 0$	66.03	60.71	54.91	48.63
		$\alpha_v = 0.5\alpha_h$	11.09	8.65	5.93	2.79		$\alpha_v = 0.5\alpha_h$	58.75	52.93	46.55	39.55
		$\alpha_v = \alpha_h$	9.72	7.08	4.14	0.47		$\alpha_v = \alpha_h$	52.29	46.12	39.28	31.67
	0.40	$\alpha_v = -\alpha_h$	-	-	-	-	0.40	$\alpha_v = -\alpha_h$	-	-	-	-

		α_v= -0.5α_h	-	10.13	9.68	7.99		α_v= -0.5α_h	-	-	-	-
		α_v= 0	11.63	9.99	7.66	5.01		α_v= 0	61.97	57.21	52.02	45.84
		α_v= 0.5α_h	10.38	8.09	5.45	2.29		α_v= 0.5α_h	55.24	49.66	43.50	36.70
		α_v= α_h	9.05	6.49	3.57	-		α_v= α_h	49.00	42.94	36.19	28.61
	0.45	α_v= -α_h	-	-	-	-	0.45	α_v= -α_h	-	-	-	-
		α_v= -0.5α_h	-	-	-	-		α_v= -0.5α_h	-	-	-	-
		α_v= 0	10.53	9.40	7.23	4.74		α_v= 0	58.02	53.54	48.70	42.19
		α_v= 0.5α_h	9.67	7.55	5.00	1.80		α_v= 0.5α_h	51.83	46.48	40.54	33.94
		α_v= α_h	8.43	5.95	3.03	-		α_v= α_h	45.95	40.03	33.37	25.81
	0.50	α_v= -α_h	-	-	-	-	0.50	α_v= -α_h	-	-	-	-
		α_v= -0.5α_h	-	-	-	-		α_v= -0.5α_h	-	-	-	-
		α_v= 0	9.56	8.13	6.77	4.46		α_v= 0	51.69	47.71	44.97	39.61
		α_v= 0.5α_h	8.97	7.04	4.58	1.24		α_v= 0.5α_h	48.48	43.38	37.67	31.28
		α_v= α_h	7.86	5.46	2.53	-		α_v= α_h	43.12	37.32	30.77	23.23
5	0	0	27.68	22.10	15.93	9.35	0	0	219.46	204.15	187.19	168.47
	0.05	α_v= -α_h	29.11	23.54	17.61	11.18	0.05	α_v= -α_h	228.93	214.00	197.48	179.32
		α_v= -0.5α_h	28.24	22.65	16.68	10.21		α_v= -0.5α_h	222.82	207.82	191.19	172.86
		α_v= 0	27.41	21.80	15.80	9.27		α_v= 0	217.01	201.94	185.18	166.68
		α_v= 0.5α_h	26.62	21.00	14.96	8.39		α_v= 0.5α_h	211.47	196.33	179.46	160.79
		α_v= α_h	25.87	20.23	14.16	7.53		α_v= α_h	206.54	190.98	173.99	155.16
	0.10	α_v= -α_h	30.07	24.74	19.06	12.94	0.10	α_v= -α_h	234.92	220.55	204.75	187.47
		α_v= -0.5α_h	28.32	22.93	17.17	10.93		α_v= -0.5α_h	222.63	208.08	192.03	174.38
		α_v= 0	26.73	21.29	15.46	9.09		α_v= 0	211.47	196.76	180.45	162.42
		α_v= 0.5α_h	25.28	19.80	13.88	7.39		α_v= 0.5α_h	201.30	186.42	169.87	151.48
		α_v= α_h	23.95	18.42	12.43	5.81		α_v= α_h	191.98	176.96	162.55	141.39
	0.15	α_v= -α_h	30.64	25.65	20.30	14.56	0.15	α_v= -α_h	238.61	224.98	210.08	193.84
		α_v= -0.5α_h	28.08	22.97	17.48	11.51		α_v= -0.5α_h	220.50	206.55	192.21	174.35
		α_v= 0	25.84	20.62	14.99	8.81		α_v= 0	204.74	190.48	174.71	157.23
		α_v= 0.5α_h	23.87	18.56	12.80	6.39		α_v= 0.5α_h	190.91	176.37	160.17	142.07
		α_v= α_h	21.12	16.72	10.83	4.18		α_v= α_h	178.65	163.85	147.23	128.55
	0.20	α_v= -α_h	30.75	26.18	21.29	15.98	0.20	α_v= -α_h	239.50	226.78	212.96	197.88
		α_v= -0.5α_h	27.56	22.78	17.61	11.96		α_v= -0.5α_h	216.71	203.42	193.84	180.07
		α_v= 0	24.83	19.86	14.46	8.48		α_v= 0	197.28	182.54	168.34	151.40
		α_v= 0.5α_h	22.47	17.35	11.75	5.41		α_v= 0.5α_h	180.67	166.52	150.71	132.93
		α_v= α_h	20.43	15.18	9.36	2.62		α_v= α_h	166.34	151.82	135.42	116.82
	0.25	α_v= -α_h	29.92	25.99	21.74	17.07	0.25	α_v= -α_h	236.11	224.49	211.79	197.98
		α_v= -0.5α_h	26.69	22.31	17.55	12.26		α_v= -0.5α_h	210.82	198.37	184.72	169.56
		α_v= 0	23.70	19.05	13.88	8.08		α_v= 0	189.14	174.01	161.44	145.07
		α_v= 0.5α_h	21.12	16.20	10.74	4.44		α_v= 0.5α_h	170.80	157.04	141.58	124.13
		α_v= α_h	19.90	13.78	8.03	0.96		α_v= α_h	155.19	140.90	124.65	106.13
	0.30	α_v= -α_h	-	23.77	20.91	17.35	0.30	α_v= -α_h	224.40	214.06	202.80	190.59
		α_v= -0.5α_h	25.17	21.38	17.18	12.37		α_v= -0.5α_h	202.45	190.85	178.05	163.95
		α_v= 0	22.44	18.33	13.24	7.65		α_v= 0	180.41	167.91	153.87	138.20
		α_v= 0.5α_h	19.81	15.10	9.79	3.46		α_v= 0.5α_h	161.24	147.93	132.82	115.73
		α_v= α_h	17.51	12.52	6.82	-		α_v= α_h	144.99	130.98	114.84	96.34
	0.35	α_v= -α_h	-	-	-	-	0.35	α_v= -α_h	-	-	-	-
		α_v= -0.5α_h	21.87	19.62	16.32	12.24		α_v= -0.5α_h	190.14	179.48	167.73	154.82
		α_v= 0	20.95	17.42	12.56	7.19		α_v= 0	171.01	156.05	145.65	130.63
		α_v= 0.5α_h	18.52	14.04	8.90	2.45		α_v= 0.5α_h	152.09	139.18	124.39	107.62
		α_v= α_h	16.23	11.37	5.70	-		α_v= α_h	135.68	121.93	105.92	87.39
	0.40	α_v= -α_h	-	-	-	-	0.40	α_v= -α_h	-	-	-	-
		α_v= -0.5α_h	-	-	-	-		α_v= -0.5α_h	171.54	162.33	152.14	140.89
		α_v= 0	19.11	16.59	11.81	6.70		α_v= 0	160.57	147.22	136.50	122.23
		α_v= 0.5α_h	17.25	13.03	8.05	1.09		α_v= 0.5α_h	143.29	130.69	116.30	99.78
		α_v= α_h	15.06	10.33	4.65	-		α_v= α_h	127.18	113.63	97.76	79.18

0.45	$\alpha_v = -\alpha_h$	-	-	-	-	0.45	$\alpha_v = -\alpha_h$	-	-	-	-
	$\alpha_v = -0.5\alpha_h$	-	-	-	-		$\alpha_v = -0.5\alpha_h$	-	-	-	120.68
	$\alpha_v = 0$	17.21	15.25	10.31	6.18		$\alpha_v = 0$	148.80	138.28	126.37	112.96
	$\alpha_v = 0.5\alpha_h$	15.97	12.06	7.25	-		$\alpha_v = 0.5\alpha_h$	134.68	122.47	108.42	92.25
	$\alpha_v = \alpha_h$	13.99	9.39	3.67	-		$\alpha_v = \alpha_h$	119.41	105.99	90.25	71.62
0.50	$\alpha_v = -\alpha_h$	-	-	-	-	0.50	$\alpha_v = -\alpha_h$	-	-	-	-
	$\alpha_v = -0.5\alpha_h$	-	-	-	-		$\alpha_v = -0.5\alpha_h$	-	-	-	-
	$\alpha_v = 0$	-	13.89	8.52	5.65		$\alpha_v = 0$	139.23	128.94	117.25	104.12
	$\alpha_v = 0.5\alpha_h$	14.66	11.12	6.50	-		$\alpha_v = 0.5\alpha_h$	126.28	114.43	100.77	84.96
	$\alpha_v = \alpha_h$	12.99	8.53	2.71	-		$\alpha_v = \alpha_h$	112.24	98.99	83.30	64.56

5. Conclusions

This study examined the effect of the pseudo-static seismic forces on the stability of a circular tunnel in cohesive-frictional soils using the upper bound theorem based on a stable-node based smoothed finite element in conjunction with the second-order cone programming. In addition, several numerical simulations were performed to assess the stability numbers' variations with changes in α_h,α_v and $\gamma D/c$ for a different combination of ϕ and H/D. Based on the results and discussion presented, the following general conclusions can be made:

1. The values of σ_s/c obtained under static conditions ($\alpha_h = 0$) using the present method agree well with the literature results reported by Yamamoto et al. (2011a) and T. Vo-Minh et al. (2017b), with the errors being within ± 5%. Numerical results reveal that the stability number values using SNS-FEM are more rapidly convergent than other numerical methods, such as FEM-T3 and ES-FEM-T3. When the fine mesh is used in the analyses, the total number of SNS-FEM variables becomes smaller than those using FEM-T3 and ES-FEM-T3, confirming the SNS-FEM approach's effectiveness when using the Mosek optimizer for solving significant sparse SOCP problems.
2. Under seismic conditions $\alpha_h > 0$ and $\alpha_v = 0$, the reduction of stability numbers is due to the seismic degradation of the shear strength of the soil, the inertia forces rising in the soil mass, and additional inertia forces associated with the surcharge. The seismic stability numbers σ_{sE}/c for all friction angles decrease with an increase in α_h, and the reduction rate increases rapidly for the higher acceleration of the earthquake. With an increase in α_h from 0 to 0.5, the reduction in the stability number has been found approximately in a range of (i) 25%-35% for $H/D = 1$, and (ii) 30%-50% for $H/D = 3$, $H/D = 5$. Furthermore, the magnitudes of stability numbers decrease with an increasing soil property $\gamma D/c$. In contrast, the stability results increase continuously with an increase in both H/D and ϕ. In some cases, H/D = 1-5, the soil property $\gamma D/c = 2$ and $\alpha_h = 0.2$, the pseudo-static seismic force in the horizontal direction is applied from left to right while the failure zones reverse to the acting of the earthquake. In these cases, the stability number becomes a negative value, implying that normal tensile stress should be applied to the ground surface to prevent collapse.
3. Under static conditions $\alpha_h = 0$ and $\alpha_v = 0$, the failure mechanism of a shallow circular tunnel is symmetrical about the vertical plane passing through the tunnel's centre. However, for $\alpha_h > 0$, circular tunnels' failure mechanisms become non-symmetrical about the vertical plane passing through the centre of the tunnel. Since the horizontal seismic force is applied from left to right, the

left horizontal failure zones from the tunnel centre are more extensive than those from the right sides. Furthermore, the size of circular tunnels' failure mechanism increases with reducing friction angle values ϕ and the failure domain is expanding continuously with an increase in both H/D and $\gamma D/c$.

4. The corrective coefficients were defined as the ratios of seismic to static stability numbers to point out the reduction in the stability of circular tunnels due to the effect of cohesion and soil inertia. For weightless soil $\gamma D/c = 0$ and $\alpha_h > 0.25$, increasing the internal angle of soil ϕ, the reduction rate of the corrective coefficients depends on cohesion and tends to decrease in all cases of H/D. On the contrary, in the case of $\gamma D/c = 1$, the reduction rate of corrective coefficients tends to increase with an increase in the internal angle of soil ϕ. Different from the tendency is due to the effect of the lateral inertia force in the soil mass to reduce the corrective coefficients of circular tunnels.
5. Based on the upper bound limit analysis using SNS-FEM, the stability results are available for the cases of $\phi \leq 35^{o}$. In addition, design tables and dimensionless charts are presented with various soil properties $\gamma D/c$ and ϕ, geometric parameters H/D and horizontal earthquake acceleration coefficient α_h for practical use in geotechnical engineering.
6. This paper investigates the effect of both horizontal and vertical components of seismic acceleration on the stability numbers σ_s/c. Corrective coefficients e_{sE} were defined as the ratios of seismic to static surcharge loadings to point out the reduction in stability of circular tunnels due to seismic effects. It is observed that positive values of α_v (upward) increase the stability numbers σ_s/c with an increasing α_h. Therefore, upward vertical acceleration increases the circular tunnel's stability. In contrast, negative values of α_v (downward) reduce the stability numbers σ_s/c with an increase in horizontal acceleration α_h and it reduces the stability of circular tunnels, geotechnical engineers need to consider this problem in the seismic preliminary design stage of circular tunnels.

Acknowledgements

This paper is part of the TPS project. The first author gratefully appreciates the support of the Foundation for Science and Technology at HUTECH University, Ho Chi Minh City, Vietnam. The second author thanks Prof. Nguyen-Thoi Trung for sharing the code and discussion on the smoothed finite element analysis. He gratefully acknowledges the financial support provided by the Dean’s Fund from Imperial College London (2017-2020).

References

Abate, G., Grasso, S., Massimino, M. R., 2019. The role of shear wave velocity and non-linearity of soil in the seismic response of a coupled tunnel-soil-above ground building system. Geosciences, 9(11), 1-25.

Abate, G., Corsico, S., Massimino, M. R., 2019. Behaviour of coupled tunnel-soil-above ground building systems in seismic conditions evaluated by means of parametric analyses. In: Proceedings of the 7th International Conference on Earthquake Geotechnical Engineering (ICEGE 2019), Italy, pp. 985-992.

Atkinson, J. H., and Potts, D. M., 1977. Stability of a shallow circular tunnel in cohesionless soils. Géotechnique, 27(2), 203-215.

Banerjee, S. K., and Chakraborty, D., 2016. Seismic stability of a long unlined circular tunnel in sloping ground. Can Geotech J., 53(8), 1346-1352.

Chakraborty, D., and Kumar, J. 2013. Stability of a long unsupported circular tunnel in soils with seismic forces. Nat Hazards, 68, 419-431.

Chen, W. F.,1975. Limit analysis and soil plasticity, Elsevier, Amsterdam, Netherlands.

Cilingir, U., Gopal Maddabushi, S. P., (2011). Effect of depth on seismic response of circular tunnels. Can. Geo. J, 48(1), 117-127.

Davis, E. H., Gunn, M. J., Mair, R. J., and Seneviratne, H. N., 1980. The stability of shallow tunnels and underground openings in cohesive material. Geotechnique, 30(4), 397-416.

Drucker, D.C., Prager, W., Greenberg, H.J., 1952. Extended limit design theorems for continuous media. Quart. Appl. Math. 9, 381-389.

Feng, H., Cui, X.Y., Li, G.Y., 2016. A stable nodal integration method with strain gradient for static and dynamic analysis of solid mechanics. Engineering Analysis with Boundary Element, 62, 78-92.

Gregor, I., Pelin, A., Wei, W., and Ronaldo, I. B., 2011. Centrifuge model test on the face stability of shallow tunnel. Acta Geotech, 6, 105-117.

Kirsch, A., 2010. Experimental investigation of the face stability of shallow tunnels in sand. Acta Geotech, 5, 43-62.

Leca, E., and Dormieux, L., 1990. Upper and lower bound solutions for the face stability of shallow circular tunnels in frictional material. Geotechnique, 40(4), 581-606.

Liu, G.R., Nguyen-Thoi, T., Nguyen-Xuan, H., Lam, K.Y., 2009. A node-based smoothed finite element method (NS-FEM) for the upper bound solution to solid mechanics problems. Computer and Structures. 87, 14-26

Liu, G.R., Chen, L., Nguyen-Thoi, T., Zeng, K.Y., Zhang, G.Y., 2010. A novel singular node-based smoothed finite element method (NS-FEM) for upper bound solutions of fracture problems. International Journal for Numerical Methods in Engineering, 83, 1466-1497.

Lyamin, A. V., and Sloan, S. W., 2000. Stability of a plane strain circular tunnel in cohesive frictional soil. In: Proceedings of the J.R. Booker Memorial Symposium, Sydney, pp. 139-153.

Lyamin, A. V., Jack, D. L., and Sloan, S.W., 2001. Collapse analysis of square tunnels in cohesive-frictional soils. In*:* Proceedings of the First Asian-Pacific Congress on Computational Mechanics, Sydney, pp. 405-414.

Mair, R. J., 1979. Centrifugal modelling of tunnel construction in soft clay. PhD thesis, Uni. of Cambridge, UK.

Makrodimopoulos, A., and Martin, C. M., 2006. Upper bound limit analysis using simplex strain elements and second-order cone programming. Int. J. for Num. and Anal. Methods in Geomechanics, 31, 835-865.

Mohapatra, D., and Kumar, J., 2019. Smoothed finite element approach for kinematic limit analysis of cohesive frictional materials. European Journal of Mechanics/A Solids, 76, 328-345.

Mosek, 2009. The MOSEK optimization toolbox for MATLAB manual. http://www.mosek.com.

Mühlhaus, H. B., 1985. Lower bound solutions for circular tunnels in two and three dimensions. Rock Mech Rock Eng, 18, 37–52.

Nguyen, H. C., 2021a. Upper bound analysis of seismic stability of tunnels using cell-based smoothed finite element. In Geotechnical Aspects of Underground Construction in Soft Ground (pp. 337-342). CRC Press.

Nguyen, H.C., 2021b. The use of adaptive smoothed finite-element limit analysis to seismic stability of tunnels. In Geotechnical Aspects of Underground Construction in Soft Ground (pp. 330-336). CRC Press.

Nguyen, H.C. and Nguyen-Son, L., 2022. A stable CS-FEM for the static and seismic stability of a single square tunnel in the soil where the shear strength increases linearly with depth. Journal of Rock Mechanics and Geotechnical Engineering.

Nguyen, H.C. and Vo-Minh, T., 2022a. Calculation of seismic bearing capacity of shallow strip foundations using the cell-based smoothed finite element method. Acta Geotechnica, pp.1-24.

Nguyen, H.C. and Vo-Minh, T., 2022b. The use of the node-based smoothed finite element method to estimate static and seismic bearing capacities of shallow strip footings. Journal of Rock Mechanics and Geotechnical Engineering, 14(1), pp.180-196.

Nguyen-Thoi, T., Vu-Do, H.C., Rabczuk, T., Nguyen-Xuan, H., 2010. A node-based smoothed finite element method (NS-FEM) for the upper bound solution to visco-elastoplastic analyses of solids using triangular and tetrahedral meshes. Computer methods in Applied Mechanics and Engineering, 199, 3005-3027.

Nguyen-Thoi, T., Liu, G.R., Nguyen-Xuan, H., Nguyen-Tran, C., 2011. Adaptive analysis using the node-based smoothed finite element method (NS-FEM). International Journal for Numerical methods in Biomedical Engineering, 27, 198-218.

Nguyen-Xuan, H., Rabczuk, T., Nguyen-Thoi, T., Tran, T.N., Nguyen-Thanh, N., 2012. Computation of limit and shakedown loads using a node-based smoothed finite element method. International Journal for Numerical Methods in Engineering, 90, 287-310.

Sahoo, J.P., Kumar, J., 2012. Seismic stability of a long unsupported circular tunnel. Comput. Geotech. 44, 109-115.

Sahoo, J.P., Kumar, J., 2014. Stability of a circular tunnel in presence of pseudostatic seismic body forces. Tunnelling and Underground Space Technology, 42, 264-276.

Seneviratne, H. N., 1979. Deformations and pore-pressures around model tunnels in soft clay. PhD thesis, Uni. of Cambridge, UK.

Sloan, S. W., and Assadi, A., 1991. Undrained stability of a square tunnel in a soil whose strength increases linearly with depth. Com. and Geotech., 12(4), 321–346.

Tang, Q., Zhang, G.Y., Liu, G.R., Zhong, Z.H., He, Z.C., 2011. A three-dimensional adaptive analysis using the meshfree node-based smoothed point interpolation method (NS-PIM). Engineering Analysis with Boundary Element, 35, 1123-1135.

Tsinidis, G., Pitilakis, K., Trikalioti, A. D., 2014. Numerical simulation of round robin numerical test on tunnels using a simplified kinematic hardening model. Acta Geotechnica, 9, 641-659.

Vo-Minh, T., Nguyen-Minh, T., Chau-Ngoc, A., Nguyen-Chanh, H., 2017a. Stability of twin circular tunnels in cohesive-frictional soil using the node-based smoothed finite element method (NS-FEM). J. of Vibroengineering, 19(1), 520-538.

Vo-Minh, T., Nguyen-Minh, T., Chau-Ngoc, A., 2017b. Upper bound limit analysis of circular tunnel in cohesive-frictional soils using the node-based smoothed finite element method. In: Proc. of the Int. Con. on Advances in Comp. Mechanics, Phu Quoc Island, Vietnam, pp.123-141.

Vo-Minh, T., Chau-Ngoc, A., Nguyen-Minh, T., and Nguyen-Chanh, H., 2018. A node-based smoothed finite element method for stability analysis of dual square tunnels in cohesive-frictional soils. Scientia Iranica, 25(3), 1105-1121.

Vo-Minh, T., Nguyen-Son, L., 2021. A stable node-based smoothed finite element method for stability analysis of two circular tunnels at different depths in cohesive-frictional soils. Comput. and Geotech., 129, 103865.

Wang, G., Cui, X.Y., Feng, H., Li, G.Y., 2015. A stable node-based smoothed finite element method for acoustic problems. Computer methods in Applied Mechanics and Engineering, 297, 348-370.

Wang, H. F., Lou, M. L., Chen, X., Zhai, Y. M., 2013. Structure-soil-structure interaction between underground structure and ground structure. Soil Dyn. Earthq. Eng., 54, 31-38.

Wilson, D.W., Abbo, A.J., Sloan, S.W., Lyamin, A.V., 2011. Undrained stability of a circular tunnel where the shear strength increases linearly with depth. Can Geotech J., 48, 1328-1342.

Wu, B.R., Lee, C.J., 2003. Ground movements and collapse mechanisms induced by tunnelling in clayey soil. Int. J. Phys. Model. Geotech, 4, 15–29.

Wu, S.C., Liu, G.R., Zhang, H.O., Xu, X., Li, Z.R., 2009. A node-based smoothed point interpolation method (NS-PIM) for three-dimensional heat transfer problems. International Journal of Thermal Sciences, 48, 1367-1376.

Yamamoto, K., Lyamin, A. V., Wilson, D. W., Sloan, S. W., and Abbo, A. J., 2011a. Stability of a circular tunnel in cohesive–frictional soil subjected to surcharge loading. Comput. and Geotech., 38(4), 504-514.

Yamamoto, K., Lyamin, A. V., Wilson, D. W., Sloan, S. W., and Abbo, A. J., 2011b. Stability of a single tunnel in cohesive–frictional soil subjected to surcharge loading. Can. Geotech. J., 48(12), 1841-1854.

Yang, F., Yang, J.S., 2010. Stability of shallow tunnel using rigid blocks and finite element upper bound solutions. Int. J. Geomech, 10 (6), 242–247.

Yang, H., Cui, X.Y., Li, S., Bie, Y.H., 2019. A stable node-based smoothed finite element method for metal forming analysis. Computational Mechanics, 63, 1147-1164.

Zi-hong, G., Xin-rong, L., Lin, L., Zhanyuan, Z., 2019. Seismic analysis of shallow tunnel collapse mechanisms with the horizontal slice method. Journal of Enggi., 4, 18-36.